# Removing ENSO-Related Variations from the Climate Record

GILBERT P. COMPO AND PRASHANT D. SARDESHMUKH

*CIRES Climate Diagnostics Center, University of Colorado, and NOAA/Earth System Research Laboratory,*
*Physical Sciences Division, Boulder, Colorado*

## ABSTRACT

An important question in assessing twentieth-century climate change is to what extent have ENSO-related variations contributed to the observed trends. Isolating such contributions is challenging for several reasons, including ambiguities arising from how ENSO itself is defined. In particular, defining ENSO in terms of a single index and ENSO-related variations in terms of regressions on that index, as done in many previous studies, can lead to wrong conclusions. This paper argues that ENSO is best viewed not as a *number* but as an evolving *dynamical process* for this purpose. Specifically, ENSO is identified with the four dynamical eigenvectors of tropical SST evolution that are most important in the observed evolution of ENSO events. This definition is used to isolate the ENSO-related component of global SST variations on a month-by-month basis in the 136-yr (1871–2006) Hadley Centre Sea Ice and Sea Surface Temperature dataset (HadISST). The analysis shows that previously identified multidecadal variations in the Pacific, Indian, and Atlantic Oceans all have substantial ENSO components. The long-term warming trends over these oceans are also found to have appreciable ENSO components, in some instances up to 40% of the total trend. The ENSO-unrelated component of 5-yr average SST variations, obtained by removing the ENSO-related component, is interpreted as a combination of anthropogenic, naturally forced, and internally generated coherent multidecadal variations. The following two surprising aspects of these ENSO-unrelated variations are emphasized: 1) a strong *cooling* trend in the eastern equatorial Pacific Ocean and 2) a nearly zonally symmetric multidecadal tropical–extratropical seesaw that has amplified in recent decades. The latter has played a major role in modulating SSTs over the Indian Ocean.

## 1. Introduction

Distinguishing anthropogenic from natural climate variations is among the most important problems in climate research today. Three kinds of natural variations need to be considered. Variations of the first kind arise from changes in external radiative forcing associated with insolation changes and volcanic eruptions. Variations of the second kind are generated through internal dynamical mechanisms of coherent long-term variability in the ocean. Natural variations of the third kind, that one may call climate noise, are associated with the incoherent low-frequency imprint of phenomena with shorter time scales. The dominant contributor to this noise is the El Niño–Southern Oscillation (ENSO). ENSO is the largest signal in the climate system on interannual

scales, but on longer scales it appears largely as noise. Because its spectrum has a long low-frequency tail, fluctuations in the timing, number, and amplitude of individual El Niño and La Niña events within, say, 50-yr intervals can give rise to substantial 50-yr trends. Such trends are inherently unpredictable. Anthropogenic and naturally forced climate changes, as well as coherent (and therefore potentially predictable) internally generated long-term climate variations, have to be measured against this ENSO-related noise background to appreciate their true significance around the globe.

Ideally, one would use ocean–atmosphere coupled climate models to estimate this background. Unfortunately, many current models have substantial errors in representing tropical variability associated with ENSO (e.g., Newman et al. 2009; Zhang and McPhaden 2006; Joseph and Nigam 2006). The dominant tropical empirical orthogonal function (EOF) pattern of sea surface temperature (SST) variability in the models deviates substantially from that in observations (Zhang and McPhaden 2006). The models also do not reproduce the frequency power

*Corresponding author address:* Gilbert P. Compo, CIRES Climate Diagnostics Center and NOAA/ESRL/Physical Sciences Division, 325 Broadway R/PSD1, Boulder, CO 80305-3328.
E-mail: compo@colorado.edu

spectrum of the amplitude of the dominant observed EOF pattern (Newman et al. 2009). This compromises estimations of the ENSO-related component from model simulations, leaving one to rely on some analysis of the observed climate record itself for this purpose.

The problem of estimating and removing ENSO-related variations from climate records has been addressed in many previous studies using a variety of methods. Penland and Matrosova (2006, hereafter PM06) discussed several difficulties with these methods. A common approach is to use a frequency bandpass filter passing periods between approximately 2 and 6 years to identify the ENSO-related variations (e.g., Parker et al. 2007; Folland et al. 1999; Lau and Weng 1999; Zhang et al. 1997). This makes the strong assumption that *all* of the SST variability in the chosen band, and *none* outside it, is associated with ENSO. This is clearly unsatisfactory, given the broadband nature of ENSO dynamics. It is not an accident that a substantial portion of decadal and longer-term climate variability has been found to be ENSO-like (e.g., Zhang et al. 1997; Alexander et al. 2002; Newman et al. 2003; Schneider and Cornuelle 2005).

Another class of ENSO-removal methods involves linear regression on the time series of some ENSO index, such as the Niño-3.4 SST index, the equatorial Pacific cold tongue index, the Southern Oscillation index, or the amplitude [i.e., principal component (PC)] of the dominant EOF pattern of tropical SST variability (e.g., Robock and Mao 1995; Kelly and Jones 1996; Cane et al. 1997; Angell 2000; Chiang and Vimont 2004; Wheeler and Hendon 2004; Thompson et al. 2008, 2009; Vyushin and Kushner 2009). The index time series is sometimes also bandpass filtered as an initial processing step. One immediate difficulty with using such single-index definitions of ENSO is that no ENSO-unrelated variations can occur in that index. If one uses the Niño-3.4 SST index, for example, then no ENSO-unrelated "global warming" signal can ever occur in the Niño-3.4 region— *by definition*. This is also clearly unsatisfactory, given climate model predictions of a significant change in this region in the late twenty-first century in response to greenhouse gas increases (e.g., Meehl et al. 2007).

There are other difficulties with following simple regression approaches, as noted by PM06. One is that not all ENSO-related variations occur in step around the globe (Alexander et al. 2002 and references therein). For example, ENSO-related SST anomalies in the tropical Indian and Atlantic Oceans typically peak several months after those in Niño-3.4 (e.g., Covey and Hastenrath 1978; Lanzante 1996; Kumar and Hoerling 2003). Using time-lagged regressions lessens the problem (Robock and Mao 1995; Angell 2000; Vyushin and Kushner 2009) but

assumes that all frequency components are maximally correlated at the same lag.

Regression onto the dominant SST PC time series is additionally problematic: it assumes that ENSO is associated with the waxing and waning of a single SST EOF pattern, which is inconsistent with observed ENSO dynamics (e.g., Penland and Sardeshmukh 1995, hereafter PS95; Wallace et al. 1998; Vimont 2005). Some investigators (e.g., Enfield and Mestas-Nuñez 1999) have addressed this limitation by regressing global SSTs onto the complex PC time series of the dominant complex EOF of global SSTs, which is associated with two SST patterns. This is a step in the right direction, but it ignores the fact that observed ENSO evolution involves at least six patterns (PS95; Penland and Matrosova 1998; PM06). A recent study by Guan and Nigam (2008) addressed this limitation by regressing global SSTs on the PC time series obtained from a rotated extended EOF (REEOF) analysis in which ENSO evolution was associated with as many as 20 patterns.

Finally, an often overlooked aspect of almost all traditional ENSO-removal methods is the implicitly assumed, but physically unjustified, orthogonality of the ENSO-related and ENSO-unrelated variations. Consider, for concreteness, the decomposition of the anomalous tropical SST state vector $\mathbf{X}(t)$ into its ENSO-related and ENSO-unrelated parts as

$$\mathbf{X}(t) = \mathbf{x}_e(t) + \mathbf{x}_n(t) \tag{1}$$

and a similar decomposition of the rest of the anomalous climate state vector $\mathbf{Y}(t)$ as

$$\mathbf{Y}(t) = \mathbf{y}_e(t) + \mathbf{y}_n(t) \approx \mathbf{A}\mathbf{x}_e(t) + \mathbf{y}_n(t), \tag{2}$$

in which, in the simplest approximation, one may assume $\mathbf{y}_e$ to be linearly related to $\mathbf{x}_e$ (bold vectors throughout the text refer to spatial patterns or fields). We stress again that there is no physical basis for assuming the orthogonality of $\mathbf{x}_n$ and $\mathbf{x}_e$, or of $\mathbf{y}_n$ and $\mathbf{y}_e$. However, the common practice of using an $\mathbf{A}$ to estimate $\mathbf{y}_e$ that is based on linear regressions of $\mathbf{Y}(t)$ on $\mathbf{x}_e(t)$ *enforces* an orthogonality of $\mathbf{y}_n$ and $\mathbf{y}_e$. Note also that $\mathbf{y}_n$ and $\mathbf{x}_n$ need not be related (if they are related at all) through the same $\mathbf{A}$ operator that links $\mathbf{y}_e$ and $\mathbf{x}_e$. However, even if they were so related and even if $\mathbf{x}_n$ were orthogonal to $\mathbf{x}_e$, this would still not make $\mathbf{y}_n$ orthogonal to $\mathbf{y}_e$ unless $\mathbf{A}$ were an orthogonal operator (i.e., $\mathbf{A}^T\mathbf{A} = c\mathbf{I}$), for which there is no physical justification. Similar comments apply to methods determining $\mathbf{y}_n(t)$ from regressions of $\mathbf{x}_n(t)$ onto $\mathbf{Y}(t)$ (e.g., Guan and Nigam 2008).

PM06 proposed an alternative method for isolating $\mathbf{x}_e$, based on the analysis of PS95, who had shown that the evolution of tropical SST anomaly fields $\mathbf{x}(t)$ in a truncated EOF space is well approximated over several seasons by the linear equation $\mathbf{x}(t + \tau) = \mathbf{G}(\tau)\mathbf{x}(t) + \boldsymbol{\varepsilon}$, where $\mathbf{G}(\tau) = \exp(\mathbf{L}\tau)$, $\mathbf{L}$ is a constant matrix, and $\boldsymbol{\varepsilon}$ is a noise vector. PS95 also showed that the development of ENSO events is well approximated by the evolution $\mathbf{x}(t) = \mathbf{G}(t)\mathbf{x}(0)$ from an "optimal" initial SST anomaly field $\mathbf{x}(0) = \boldsymbol{\phi}_1$ identified with the dominant right singular vector $\boldsymbol{\phi}_1$ of $\mathbf{G}$ ($\tau = 7$ months). This evolution leads to a mature ENSO pattern and subsequent decay, as observed. PS95 stressed the pattern-changing aspect of this evolution: $\boldsymbol{\phi}_1$ is distinct from the mature ENSO pattern that it evolves into. Furthermore, this pattern-changing evolution occurs almost entirely within a linear vector space spanned by a three-mode subset $\{\mathbf{U}_k\}$ of the eigenmodes of $\mathbf{L}$; that is, $\boldsymbol{\phi}_1$ is well approximated by a linear combination of this subset. PM06 exploited this fact to define the evolving ENSO-related part $\mathbf{x}_e(t)$ of tropical SST series $\mathbf{x}(t)$ as $\mathbf{x}_e(t) = \sum \alpha_k(t)\mathbf{U}_k$.

Our principal goal in this paper is to isolate the ENSO-related component of global SST variations on a month-by-month basis in the 136-yr (1871–2006) Hadley Centre Sea Ice and Sea Surface Temperature (HadISST) data set (Rayner et al. 2003) using an extended form of PM06's patterns-based filter. We define the extratropical portions $\mathbf{y}_e$ of the ENSO-related extratropical SST anomaly fields as those that are linked to the tropical portions $\mathbf{x}_e$ through the so-called "atmospheric bridge" (Alexander et al. 2002). This link is established through relatively rapid extratropical atmospheric responses to tropical SST changes and the subsequent generation, by the associated altered surface heat fluxes, of extratropical SST changes. We estimate the effective "bridge" operator $\mathbf{A}$ empirically, from linear regressions of extratropical SSTs onto tropical SSTs on interannual time scales, and separately for each month of the year (as explained later, this avoids the problem of the false imposition of orthogonality between $\mathbf{y}_e$ and $\mathbf{y}_n$ alluded to above). We then use this operator to estimate the ENSO-related extratropical SST anomaly field $\mathbf{y}_e$ associated with the ENSO-related tropical field $\mathbf{x}_e$ in each month of the 136-yr dataset. Merging this extratropical field with the tropical field yields the ENSO-related global SST anomaly field in each month of the dataset.

Removing the ENSO-related anomaly fields from the full SST anomaly fields can substantially alter one's perception of multidecadal SST variability and long-term SST trends around the globe, as will become evident in the following sections. Figure 1 provides a preview. The black curve shows the time series of globally averaged
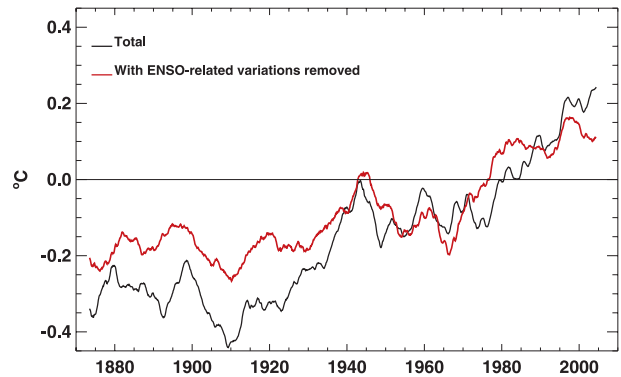


FIG. 1. Time series of the global ocean average surface temperature anomaly (black curve) and its ENSO-unrelated component determined using the ENSO patterns filter (red curve). A 10-yr running mean has been applied to both series. Anomalies are relative to a 1949–2004 climatology.

10-yr running mean SST anomalies in the HadISST dataset. The red curve shows the same series after its ENSO-related components are removed. The modification is appreciable, not just on decadal scales but even to the long-term trend. The original series has an 1871–2006 trend of ~0.05 K decade$^{-1}$, consistent with Rayner et al.'s (2003) estimate. After removal of the ENSO-related components, that trend is reduced to ~0.03 K decade$^{-1}$.

Section 2 provides further justification and some important details of our method for isolating $\mathbf{x}_e$ using a dynamical ENSO patterns filter. Our preference for a filter based on *dynamical* rather than *statistical* ENSO patterns is partly motivated by evidence that the basic *dynamics* of ENSO, as encapsulated in those eigenmodes of $\mathbf{L}$ that are most important in the evolution of ENSO events, have remained nearly constant over the past 136 years, even if the *statistics* of ENSO have not. Indeed a statistical-patterns-based filter requires an even stronger assumption that the covariance structure of the full tropical SST anomaly fields $\mathbf{X}(t)$, and not just their ENSO-related parts $\mathbf{x}_e(t)$, have remained constant over the past 136 years, which is harder to justify in a changing climate. Section 3 describes our procedure for estimating the extratropical portions $\mathbf{y}_e$ of the ENSO-related SST anomaly fields. Section 4 presents some surprising results obtained after removing the ENSO-related anomaly fields from the full anomaly fields in the HadISST dataset, including the effects on long-term trends and on the dominant global patterns of low-frequency (5-yr running mean) SST variations. Evidence that the basic dynamics of ENSO have not changed appreciably in the last 136 years is presented in section 5, and a discussion and concluding remarks follow in section 6.

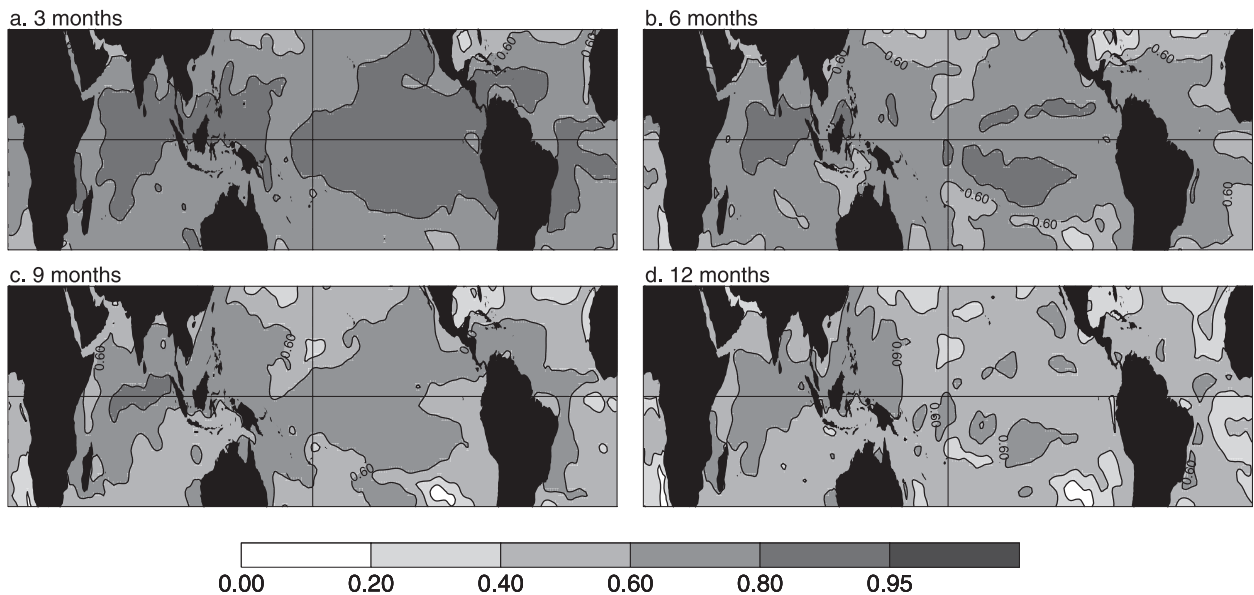Anomaly Correlation Predicting Tropical SST (1949-2004)



FIG. 2. Maps of the local anomaly correlation between observed and predicted seasonal SST anomalies using the linear inverse model prediction, Eq. (4). Maps are shown for forecast lead times of (a) 3 months, (b) 6 months, (c) 9 months, and (d) 12 months. Correlations are computed over the period 1949–2004. The contour interval is 0.2, with a 0.95 contour added.

## 2. Tropical dynamical ENSO patterns filter

As mentioned above, the ENSO pattern filter (EPF) developed by PM06 determines the ENSO-related portion $\mathbf{x}_e(t)$ of tropical SST anomaly fields as $\mathbf{x}_e(t) = \sum \alpha_k(t)\mathbf{U}_k$, where $\{\mathbf{U}_k\}$ is a particular subset of the eigenmodes of the matrix $\mathbf{L}$ in the linear model

$$\frac{d\mathbf{x}(t)}{dt} = \mathbf{L}\mathbf{x}(t) + \boldsymbol{\xi}(t), \qquad (3)$$

where $\boldsymbol{\xi}(t)$ is noise that is white in time but not necessarily in space. The forward solution of (3),

$$\mathbf{x}(t + \tau) = \exp(\mathbf{L}\tau)\mathbf{x}(t) + \varepsilon = \mathbf{G}(\tau)\mathbf{x}(t) + \varepsilon, \qquad (4)$$

describes tropical SST evolution over several seasons. Here $\mathbf{L}$ is estimated using the observed lag-covariance matrices $\mathbf{C}(\tau) = \langle \mathbf{x}(t + \tau) \, \mathbf{x}(t)^{\mathrm{T}} \rangle$ at two lags, $\tau = 0$ and $\tau = \tau_o$, as

$$\mathbf{L} = \frac{1}{\tau_o} \ln\{\mathbf{C}(\tau_o)\mathbf{C}(0)^{-1}\}, \qquad (5)$$

following the linear inverse modeling (LIM) procedure described, for example, in Penland and Magorian (1993) and PS95. Such a linear approximation can also be consistently derived from forward dynamical models of the coupled ocean–atmosphere system (PS95) and has

the advantage of correctly representing the observed statistics, not only at the training lag $\tau_o$ but at other lags as well (PS95). That linear inverse models can capture the dynamics of forward models was also shown more generally by Garcia and Penland (1991), who showed that a LIM could recover the linearized Navier–Stokes equations from Monte Carlo simulations of explicitly resolved gas particle interactions.

We applied the linear inverse modeling procedure to the 1949–2004 HadISST data, taking care to cross-validate the results (see appendix A). Maps of the cross-validated local anomaly correlation skill for forecast lead times of $\tau = 3, 6, 9,$ and 12 months show that (4) successfully captures the SST evolution in all tropical ocean basins at lead times of up to a year (Fig. 2). Nearly identical skills were obtained (not shown) with $\mathbf{L}$ operators estimated using $\tau_o = 6$ months and $\tau_o = 9$ months in (5), further attesting to the validity of (3) and (4).

As in PS95, we found that ENSO development is well described by the evolution $\mathbf{x}(t) = \mathbf{G}(t)\mathbf{x}(0)$ from an "optimal" initial condition $\mathbf{x}(0) = \boldsymbol{\phi}_1$ to a mature ENSO condition $\mathbf{x}(8) = \mathbf{G}(8)\boldsymbol{\phi}_1 = \gamma_1\boldsymbol{\psi}_1$ after 8 months, where $\boldsymbol{\phi}_1$ and $\boldsymbol{\psi}_1$ are the normalized dominant right and left singular vectors of $\mathbf{G}$ (8 months), respectively, and $\gamma_1$ is the associated singular value. The spatial patterns of $\boldsymbol{\phi}_1$ and $\boldsymbol{\psi}_1$ are shown in Fig. 3. They strongly resemble those obtained in previous studies using different datasets and domains (PS95; Penland and Matrosova 1998; PM06;
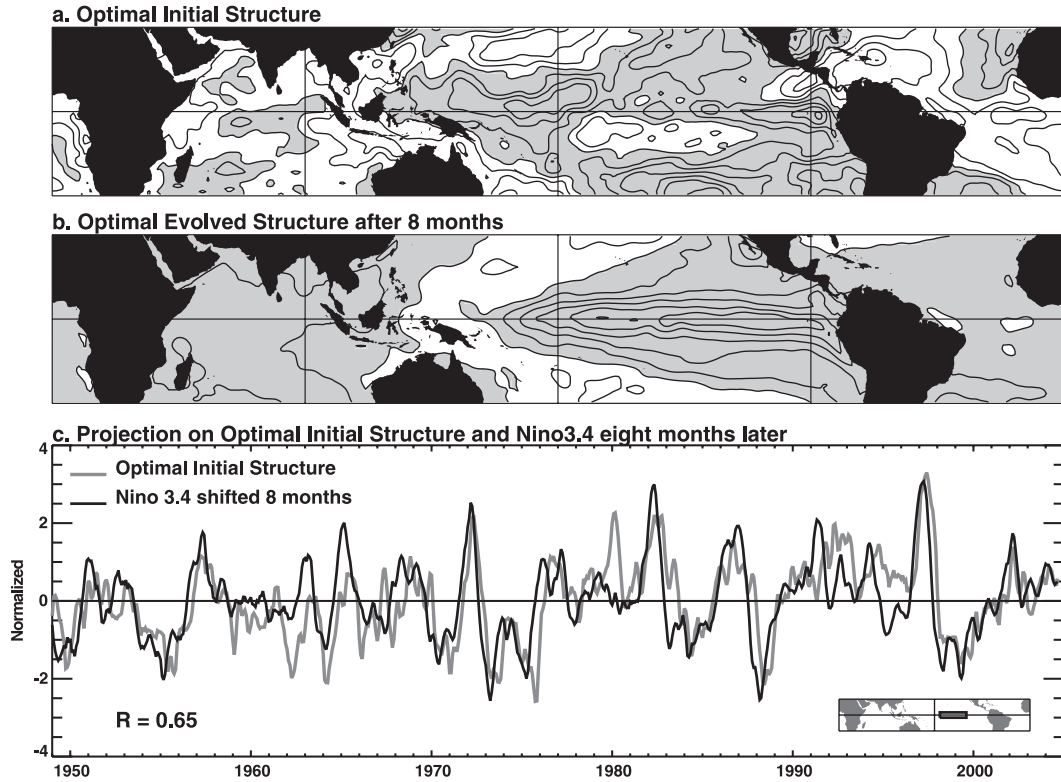
**a. Optimal Initial Structure**



**b. Optimal Evolved Structure after 8 months**



**c. Projection on Optimal Initial Structure and Nino3.4 eight months later**



FIG. 3. (a) The optimal initial SST anomaly structure that evolves into (b) the optimal "final" structure after eight months. Each field is normalized to unity. Contour interval is 0.005. Shading is arbitrary and is the same sign in both panels. (c) Time series of the projection of the optimal initial structure onto the observed SST anomalies (gray curve) and Niño-3.4 time series shifted backward eight months (black curve). Both series have been normalized by their respective standard deviations. The correlation between the gray and black series is 0.65.

Alexander et al. 2008). Figure 3c confirms that the projection of $\mathbf{x}(t)$ on $\boldsymbol{\phi}_1$ is a good predictor of Niño-3.4 SST eight months later. The 8-month lead correlation of 0.65 is much higher than, for example, the 8-month lead correlation of $-0.2$ obtained using the projection of $\mathbf{x}(t)$ on the dominant SST EOF as the predictor.

The particular insight of PM06 was to use the development from $\boldsymbol{\phi}_1$ as a basis for *defining* ENSO as a stochastically perturbed evolving dynamical *process*. Specifically, they defined the evolving ENSO-related component $\mathbf{x}_e(t)$ of the evolving tropical SST anomaly fields $\mathbf{x}(t)$ as $\mathbf{x}_e(t) = \sum \alpha_k(t)\mathbf{U}_k$, where $\{\mathbf{U}_k\}$ is that subset of the eigenvectors of $\mathbf{L}$ that contributes most to the structure of $\boldsymbol{\phi}_1$. In other words, the ENSO-related evolution is defined as the projection of Eq. (4) in this eigenvector subspace. Importantly, this does not require ENSO events to develop *precisely* from $\boldsymbol{\phi}_1$ in all cases, which of course they do not.

The evolution associated with each ENSO-relevant eigenmode of $\mathbf{L}$ may be conveniently expressed and visualized in terms of the corresponding eigenmodes of $\mathbf{G}(\tau) = \exp(\mathbf{L}\tau)$. The eigenvectors of $\mathbf{G}(\tau)$ are identical to the eigenvectors $\mathbf{U}_k$ of $\mathbf{L}$, and the eigenvalues are $\exp(\beta_k\tau)$, where $\beta_k = \sigma_k + i\omega_k$ are the corresponding eigenvalues of $\mathbf{L}$. Since $\mathbf{G}$ is real, its eigenvectors and eigenvalues occur in complex conjugate pairs. These pairs can be combined into a single real modal solution $\mathbf{x}_k(t)$ as

$$\mathbf{x}_k(t) = \{\mathbf{a}_k \cos\omega_k t + \mathbf{b}_k \sin\omega_k t\} \exp(\sigma_k t), \quad (6)$$

where $\mathbf{a}_k$ and $\mathbf{b}_k$ are real vectors with $\mathbf{a}_k^{\mathrm{T}}\mathbf{b}_k = 0$, $\mathbf{a}_k^{\mathrm{T}}\mathbf{a}_k = 1$, and $\mathbf{b}_k^{\mathrm{T}}\mathbf{b}_k \geq 1$ (see, e.g., Borges and Sardeshmukh 1995; PS95). Without the exponential decay factor, the mode traces out an ellipse in the space spanned by $\mathbf{a}_k$ and $\mathbf{b}_k$ from the minor axis $\mathbf{a}_k$ to the major axis $\mathbf{b}_k$, then to $-\mathbf{a}_k$ and $-\mathbf{b}_k$, and then back to $\mathbf{a}_k$. The *e*-folding decay time of each mode is defined as $-1/\sigma_k$, its period as $2\pi/\omega_k$, and its effective time scale as $1/|\beta_k|$. As the operator $\mathbf{L}$ is not self-adjoint, its eigenvectors $\mathbf{U}$ are not orthogonal. Many studies using both inverse and forward dynamical models have found that the eigenvectors of the dynamical operator describing the evolution of the coupled tropical ocean–atmosphere system are nonorthogonal (e.g., PS95;
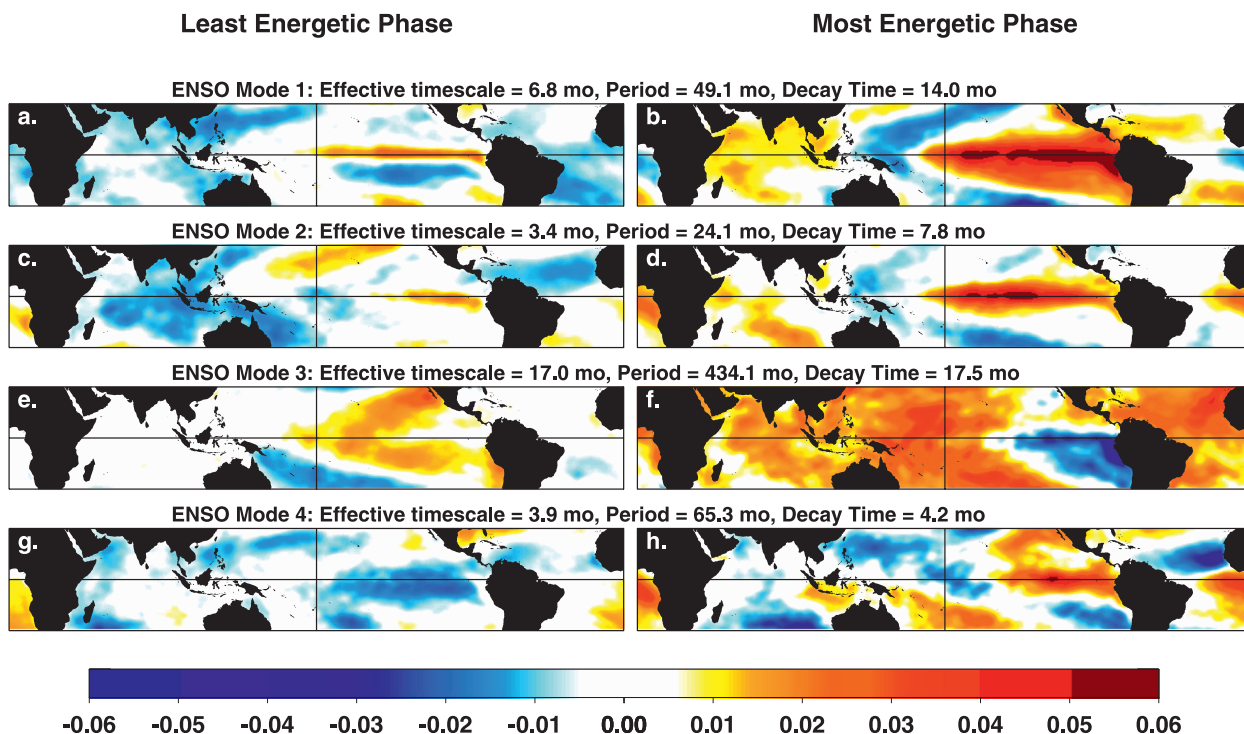
**Least Energetic Phase**                              **Most Energetic Phase**

ENSO Mode 1: Effective timescale = 6.8 mo, Period = 49.1 mo, Decay Time = 14.0 mo

ENSO Mode 2: Effective timescale = 3.4 mo, Period = 24.1 mo, Decay Time = 7.8 mo

ENSO Mode 3: Effective timescale = 17.0 mo, Period = 434.1 mo, Decay Time = 17.5 mo

ENSO Mode 4: Effective timescale = 3.9 mo, Period = 65.3 mo, Decay Time = 4.2 mo



-0.06  -0.05  -0.04  -0.03  -0.02  -0.01  0.00  0.01  0.02  0.03  0.04  0.05  0.06

FIG. 4. (left) Least energetic and (right) most energetic phases of the four dynamical ENSO modes used for defining the ENSO-related tropical SST variations. The modes are ordered according to the projection of their adjoint onto the optimal initial structure shown in Fig. 3a. Each mode's effective time scale $1/|\beta|$ is indicated. Each mode evolves from (left) the least energetic phase **a** to (right) the most energetic phase **b**, then to $-$**a**, and then to $-$**b** with the indicated period $2\pi/\omega$ while decaying with the indicated decay time scale $-1/\sigma$. The **a** phase is normalized to unity in the left panel. Note that the **a** and **b** phases of each mode are spatially orthogonal to each other by construction.

Penland and Matrosova 1998; Moore and Kleeman 1999; Thompson and Battisti 2000; Alexander et al. 2008; Newman et al. 2009). As such, nonorthogonality should be an important feature of any pattern-based definition of ENSO.

Following the objective procedure described in appendix B yielded a subset of four ENSO-relevant eigenmodes of our LIM. The least energetic spatial structure **a** and most energetic spatial structure **b** associated with each mode (6) are shown in Fig. 4, along with the effective time scale, period, and decay time. The associated amplitude time series $\alpha_k(t)$ (obtained by projecting $\mathbf{x}(t)$ on the corresponding adjoint eigenvectors $\mathbf{V}_k$) are shown in Fig. 5. ENSO mode 1 corresponds very closely to the PS95 "46 month" mode. The other modes are difficult to compare directly with previous studies—mainly because their real and imaginary parts were shown at arbitrary phases in those studies, rather than at their "least energetic" and "most energetic" phases as in (6).

Our ENSO modes 1 and 2 are readily identifiable with canonical ENSO evolution, each developing from weak warm anomalies in the eastern equatorial Pacific

into strong warm anomalies there 4–12 months later. Modes 1, 2, and 4 are associated with the previously identified quasi-4-yr, 2-yr, and 5-yr to 6-yr periodicities of ENSO (PS95; Moron et al. 1998). Modes 3 and 4 have longer periods but relatively fast decay times, so one does not expect to see more than about a quarter of the implied oscillation in individual realizations. Even so, these modes contribute to the overall evolution from $\phi_1$ to $\psi_1$. Together with modes 1 and 2, they help to explain the westward and eastward propagation of ENSO events (PS95) and also ENSO events of different "flavors" (e.g., Fu et al. 1986; Trenberth and Smith 2006).

Correlations among the modal amplitude time series in Fig. 5 are listed in Table 1. While most of the amplitude time series explain less than 1% of the variance of other series, at least one phase of each mode has a significant correlation with a phase of another mode. These correlations reflect the nonorthogonality of these dynamically relevant structures.

Having determined the ENSO-relevant eigenmodes, the ENSO-related parts $\mathbf{x}_e(t)$ of the tropical SST anomaly fields $\mathbf{x}(t)$ were determined as
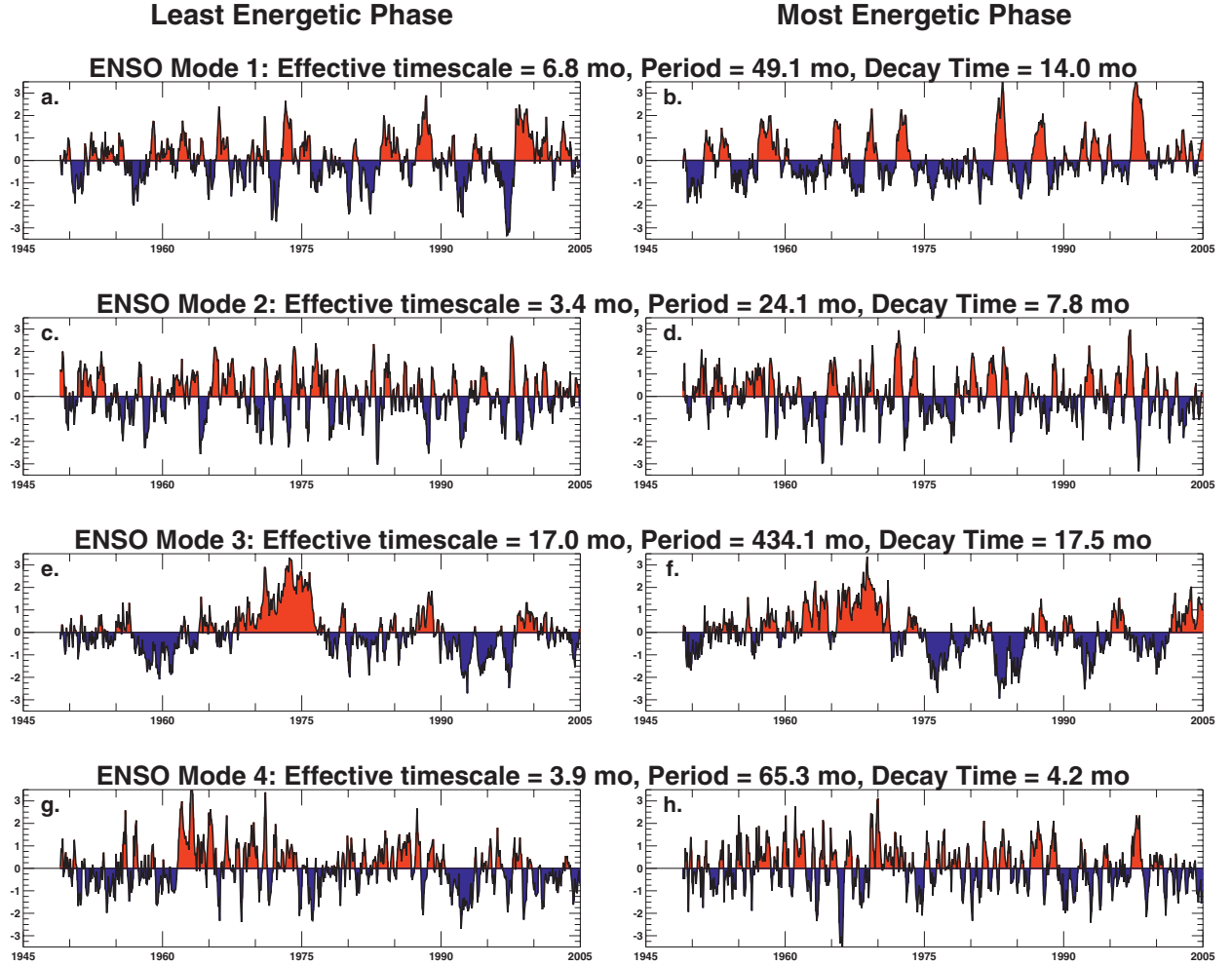
## Least Energetic Phase          Most Energetic Phase

### ENSO Mode 1: Effective timescale = 6.8 mo, Period = 49.1 mo, Decay Time = 14.0 mo

### ENSO Mode 2: Effective timescale = 3.4 mo, Period = 24.1 mo, Decay Time = 7.8 mo

### ENSO Mode 3: Effective timescale = 17.0 mo, Period = 434.1 mo, Decay Time = 17.5 mo

### ENSO Mode 4: Effective timescale = 3.9 mo, Period = 65.3 mo, Decay Time = 4.2 mo



FIG. 5. Time series from 1949 to 2004 associated with the (left) least energetic and (right) most energetic phases of the four dynamical ENSO modes from Fig. 4. Each mode's effective time scale, period, and decay time are indicated. All series have been normalized to unit standard deviation.

$$\mathbf{x}_e(t) = \sum_{k=1}^{4} \alpha_k(t)\mathbf{U}_k = \sum_{k=1}^{4} [\mathbf{V}_k^{\mathrm{T}}\mathbf{x}(t)]\mathbf{U}_k, \qquad (7)$$

and the ENSO-unrelated parts as the departures

$$\mathbf{x}_n(t) = \mathbf{X}(t) - \mathbf{x}_e(t) \qquad (8)$$

of the *full* (i.e., untruncated) SST anomaly fields $\mathbf{X}(t)$ from $\mathbf{x}_e(t)$. Note that, by construction, $\mathbf{x}_e(t)$ in (7) preserves the observed time evolution of the ENSO modes and their constructive interference as observed during the development of El Niño and La Niña events.

## 3. Extratropical ENSO-related variations

We define the ENSO-related parts $\mathbf{y}_e(t)$ of the extratropical SST anomaly fields $\mathbf{Y}(t)$ to be those that are linearly linked to $\mathbf{x}_e(t)$ as $\mathbf{y}_e(t) = \mathbf{A}\mathbf{x}_e(t)$, where $\mathbf{A}$ is a linear atmospheric bridge operator. As stated earlier, this atmospheric bridge is established through relatively rapid extratropical atmospheric responses to tropical SST changes and the subsequent generation, by their associated altered surface heat fluxes, of extratropical SST changes. We estimated $\mathbf{A}$ empirically, but bearing in mind the discussion following Eq. (2), not by regressing $\mathbf{Y}(t)$ on $\mathbf{x}_e(t)$ but, instead, by regressing bandpass filtered variations $\mathbf{y}_b(t)$ of $\mathbf{Y}(t)$ in the 2–72-month period band on similarly filtered simultaneous variations $\mathbf{x}_b(t)$ of $\mathbf{X}(t)$. We did this separately for 3-month seasons centered on each month of the annual cycle, obtaining and using 12 distinct $\mathbf{A}$ matrices in all. Having determined $\mathbf{y}_e(t)$ using these $\mathbf{A}$ matrices, we then determined the ENSO-unrelated parts $\mathbf{y}_n(t)$ as $\mathbf{y}_n(t) = \mathbf{Y}(t) - \mathbf{y}_e(t)$.

The rationale for the above procedure was as follows. First, since we define $\mathbf{y}_e(t)$ to be the relatively fast extratropical SST response to $\mathbf{x}_e(t)$ through the atmospheric

TABLE 1. Simultaneous cross-correlations of ENSO mode amplitude time series from 1949 to 2004 HadISST data. For each mode, **a** is the least energetic phase and **b** is the most energetic phase corresponding to Figs. 4 and 5. Assuming 3 degrees of freedom per year for seasonally averaged data, correlations of less than 0.16 are not statistically significant at the 5% level. Correlations in bold are statistically significant above the 5% level. From the binomial theorem, six significant correlations are expected in 1.6% or fewer sets of 28 tests.

| | | Mode 1 | | Mode 2 | | Mode 3 | | Mode 4 | |
|---|---|---|---|---|---|---|---|---|---|
| | | $\mathbf{a}_1$ | $\mathbf{b}_1$ | $\mathbf{a}_2$ | $\mathbf{b}_2$ | $\mathbf{a}_3$ | $\mathbf{b}_3$ | $\mathbf{a}_4$ | $\mathbf{b}_4$ |
| Mode 1 | $\mathbf{a}_1$ | 1 | −0.05 | −0.02 | **−0.47** | **0.35** | 0.10 | 0.08 | −0.13 |
| | $\mathbf{b}_1$ | | 1 | 0.07 | 0.06 | −0.04 | −0.02 | 0.03 | **0.21** |
| Mode 2 | $\mathbf{a}_2$ | | | 1 | 0.04 | −0.03 | 0.08 | 0.07 | −0.07 |
| | $\mathbf{b}_2$ | | | | 1 | −0.11 | −0.07 | 0.02 | −0.02 |
| Mode 3 | $\mathbf{a}_3$ | | | | | 1 | 0.09 | **0.18** | 0.06 |
| | $\mathbf{b}_3$ | | | | | | 1 | **0.34** | −0.09 |
| Mode 4 | $\mathbf{a}_4$ | | | | | | | 1 | **0.34** |
| | $\mathbf{b}_4$ | | | | | | | | 1 |

bridge mechanism, we expect the matrix **A** linking them to be the same as that linking *all* relatively fast extratropical SST variations to *all* relatively fast tropical SST variations. Hence our estimation of **A** through regressions of $\mathbf{y}_b(t)$ on $\mathbf{x}_b(t)$. An important benefit of using such an **A** is that we do not automatically impose a false orthogonality between $\mathbf{y}_e(t)$ and $\mathbf{y}_n(t)$. Second, since **A** is essen-

tially a matrix of sensitivities of the fast extratropical SST responses to tropical SST changes, then given that those sensitivities vary from season to season (Newman and Sardeshmukh 1998; Barsugli et al. 2006) it is desirable to use a seasonally varying **A** for realistic estimations of $\mathbf{y}_e$.

To minimize edge effects when merging $\mathbf{y}_e(t)$ with $\mathbf{x}_e(t)$ to construct the global ENSO-related SST anomaly fields, we actually determined **A** as the appropriate submatrix of a larger regression matrix $\tilde{\mathbf{A}}$ linking the *global* bandpass filtered SSTs $\tilde{\mathbf{y}}_b$ to $\mathbf{x}_b$. We estimated this $\tilde{\mathbf{A}}$ separately for each 3-month season in truncated spaces of the seasonally dependent EOFs of $\mathbf{x}_b$ and $\tilde{\mathbf{y}}_b$, retaining 20 and 15 EOFs, respectively, of these fields in each season. The truncation to 15 EOFs was chosen after an extensive cross-validation exercise using the 1949–2004 data, withholding 8 years of data per cross-validation set for all EOF truncations between 2 and 28. The 15-EOF truncation yielded the largest cross-validated hindcast skill of $\mathbf{y}_b$ given $\mathbf{x}_b$, in terms of both local anomaly correlation and rms error averaged over all seasons and extratropical regions. Figure 6 shows, for this optimal 15-EOF truncation, the fractional variance of $\mathbf{y}_b$ explained by $\mathbf{x}_b$, averaged over all seasons. The tropical variations evidently account for more than 10% of the extratropical variance almost everywhere and more than 50% of the variance over substantial areas.

To generate the global ENSO-related fields, we first generated a preliminary set of global fields $\tilde{\mathbf{y}}_e = \tilde{\mathbf{A}}\mathbf{x}_e$, which were very close but not identical to $\mathbf{x}_e$ in the
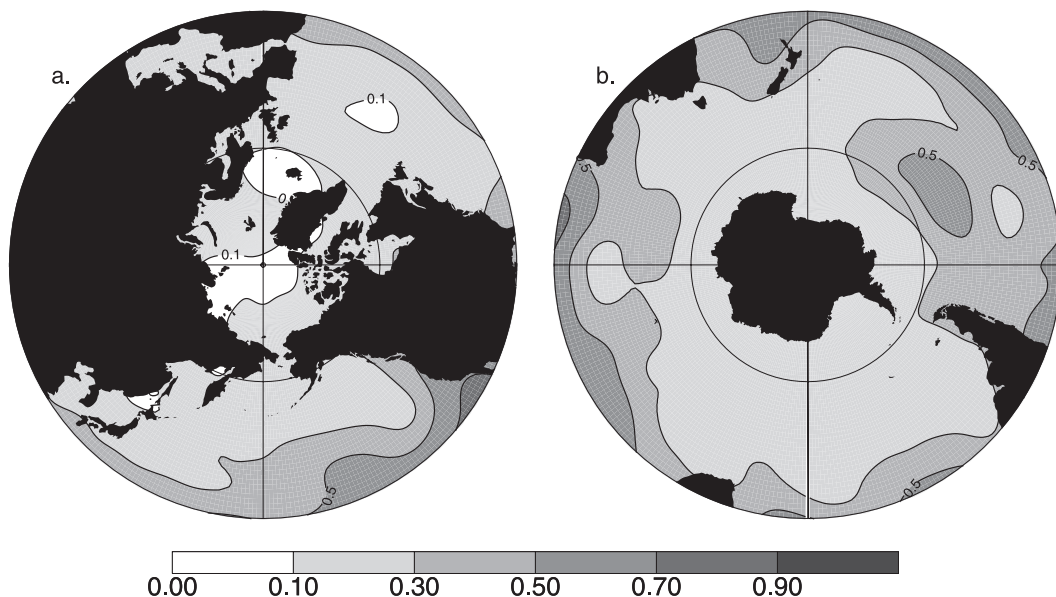


FIG. 6. Fraction of variance of bandpass filtered extratropical SST anomalies explained by similarly bandpass filtered tropical SST anomalies using the atmospheric bridge operator **A** in the (a) Northern Hemisphere and (b) Southern Hemisphere. All data were bandpass filtered using a Morlet wavelet filter with a response between 2 and 72 months. Contour interval is 0.2.
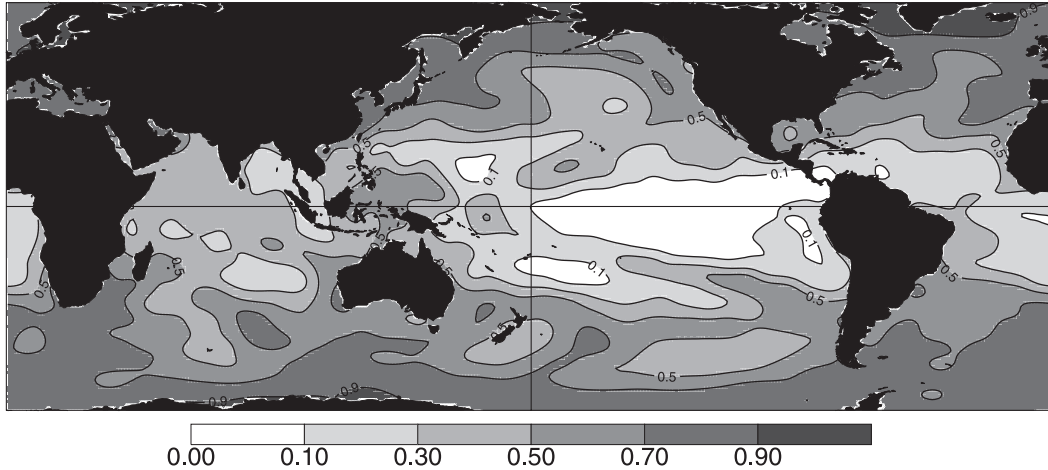
FIG. 7. Variance of ENSO-unrelated seasonal SST anomalies normalized by the total local seasonal SST anomaly variance using HadISST data from 1949 to 2004. Contour interval is 0.2.

tropics. We then created the final set $\mathbf{z}_e(t)$ by merging $\tilde{\mathbf{y}}_e$ with $\mathbf{x}_e$ as

$$\mathbf{z}_e(t) = (1 - w)\tilde{\mathbf{y}}_e(t) + w\mathbf{x}_e(t) \qquad (9)$$

using a cosine taper function $w$ decreasing from a constant value of 1 equatorward of 24.5° to zero poleward of 30.5°. The global ENSO-unrelated variations were then determined as departures of the full global SST anomaly fields $\mathbf{Z}(t)$ from $\mathbf{z}_e(t)$ as

$$\mathbf{z}_n(t) = \mathbf{Z}(t) - \mathbf{z}_e(t). \qquad (10)$$

The variance of seasonal $\mathbf{z}_n(t)$ is shown in Fig. 7 at each grid point as a fraction of the variance of seasonal $\mathbf{Z}(t)$. The ENSO-unrelated SST variations account for more than 10% of the variance of seasonal SST anomalies throughout most of the tropics, a notable exception being the region of large ENSO-related variability in the eastern Pacific. The ENSO-unrelated variations account for more than 50% of the seasonal SST variance over large portions of the extratropics during this period.

## 4. Results

We now present the results obtained after removing the ENSO-related component from the full SST anomaly fields in the HadISST dataset, including the effects on long-term trends and the dominant global patterns of low-frequency (5-yr running mean) SST variations. We also consider how removing the ENSO-related component affects the time series of various low-frequency SST indices, such as the Atlantic multidecadal oscillation (AMO) index, associated with climate variability and change.

### a. Long-term SST trends

Figure 8a shows that almost all ocean basins have warmed over the 1871–2006 period. This is in general agreement with other estimates (e.g., Hansen et al. 2006). The map shows that the warming has not been spatially uniform. The warming trend pattern for a shorter period of 1901–2005 is similar to that in Fig. 8a, but with somewhat larger amplitudes (see, e.g., Hegerl et al. 2007 and appendix C). The ENSO-related contribution to the 1871–2006 trend, obtained using (9), is shown in Fig. 8b. Not unexpectedly, it is largest in the eastern tropical Pacific and negative in parts of the North and South Pacific, consistent with the "low-frequency tail" of ENSO. More surprisingly, it also accounts for an appreciable fraction of the total warming trend in Fig. 8a in many other regions.

The ENSO-unrelated part of the 1871–2006 trend, obtained using (10), is shown in Fig. 8c. It accounts for a large fraction of the total warming trend, especially outside the tropics. The situation is much less clear in the tropics, especially in the eastern tropical Pacific where Fig. 8c shows a large ENSO-unrelated *cooling* trend. This result is surprising, but broadly consistent with the results of Cane et al. (1997) and Lau and Weng (1999) obtained using different observational datasets and analysis techniques and those of Guan and Nigam (2008) using the same HadISST dataset and the REEOF analysis technique.

Estimates of SST trends vary among reconstruction datasets (Karnauskas et al. 2009; Vecchi and Soden 2007). Nonetheless, appendix C shows that repeating our analysis using four different recent reconstructions yields broadly similar ENSO-unrelated SST trends, including a cooling trend in the eastern Pacific, despite differences

(a) Observed trend of Global Sea Surface Temperature (1871-2006) °C/50 yr

(b) ENSO-related component of observed trend
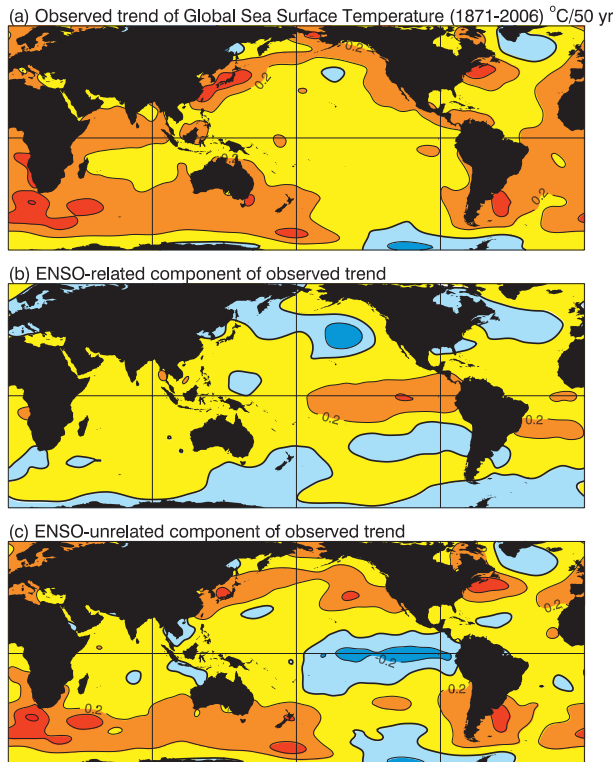
(c) ENSO-unrelated component of observed trend

FIG. 8. Global maps of linear trends over 1871–2006 of (a) the full HadISST SST anomalies, (b) the ENSO-related anomalies, and (c) the ENSO-unrelated anomalies. Contour interval is 0.2°C change per 50 years. The zero contour is thickened.



(a) Observed trend of Global Sea Surface Temperature (1949-2006) °C/50 yr

(b) ENSO-related component of observed trend

(c) ENSO-unrelated component of observed trend

FIG. 9. As in Fig. 8 but for trends over 1949–2006.

in the details of the total SST trend. A cooling trend in the eastern Pacific has been hypothesized to be a coupled response to uniform radiative forcing (Clement et al. 1996; Cane et al. 1997). Notably, such a cooling response is not produced in comprehensive coupled climate models, although it has been found in ocean models subjected to uniform radiative and enhanced absorbed shortwave forcing (Seager and Murtugudde 1997; Sweeney et al. 2005).

As is well known, the global warming trend since the late nineteenth century has not been constant but has varied considerably on multidecadal time scales (e.g., Hegerl et al. 2007). It is therefore important to construct versions of Fig. 8 for more recent periods in which the warming appears to have accelerated. Figure 9 shows the total, ENSO-related, and ENSO-unrelated SST trends over the 1949–2006 period in the same format as Fig. 8 and on the same scale. The generally larger trends in Fig. 9a compared to Fig. 8a are consistent with previous estimates using different datasets (e.g., Knutson et al. 2006). Nonetheless, the same overall conclusions may be drawn from Fig. 9 concerning the relative contributions of the ENSO-related and ENSO-unrelated trends to the total
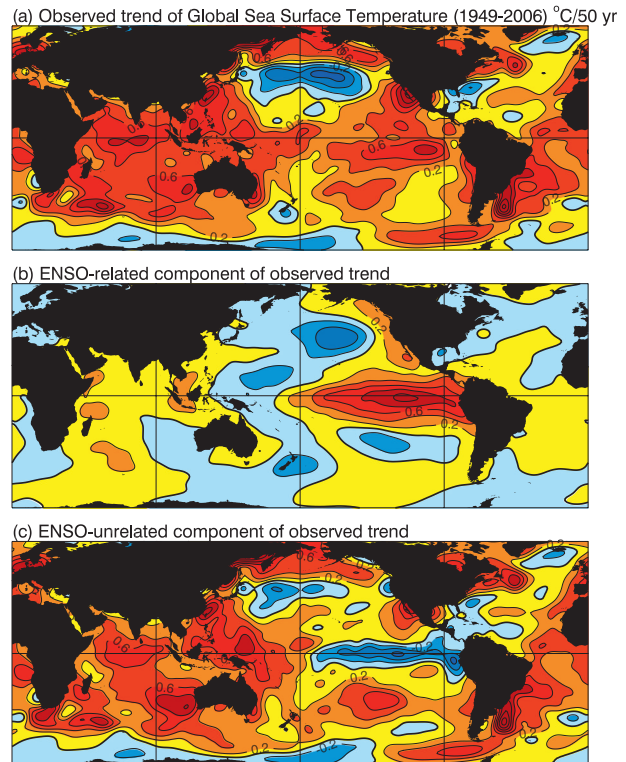
trend even over this shorter more recent period. This is partly because the ENSO-related trend is also larger in Fig. 9b than in Fig. 8b and remains generally reminiscent of the low-frequency tail of ENSO.

The ENSO-unrelated part of the 1949–2006 trend is shown in Fig. 9c. Its generally similar pattern, but weaker amplitude, compared to the observed trend in Fig. 9a suggests that it accounts for approximately two-thirds of the observed trend in most regions. The interesting ENSO-unrelated cooling trend in the eastern equatorial Pacific now appears with even larger amplitude than in Fig. 8c but is more meridionally confined. It is tempting to speculate that such a cooling is dynamically consistent with an enhancement of surface easterlies and equatorial upwelling over the eastern Pacific in response to the strong ENSO-unrelated recent warming of the Indian and west Pacific Oceans.

### b. Dominant patterns of low-frequency SST variations

Linear trend maps such as Figs. 8 and 9 fail to capture the detailed structures of observed multidecadal and longer-term variations (e.g., Parker et al. 2007 and references therein). An EOF analysis can be more revealing in this regard. The left panels of Fig. 10 show the
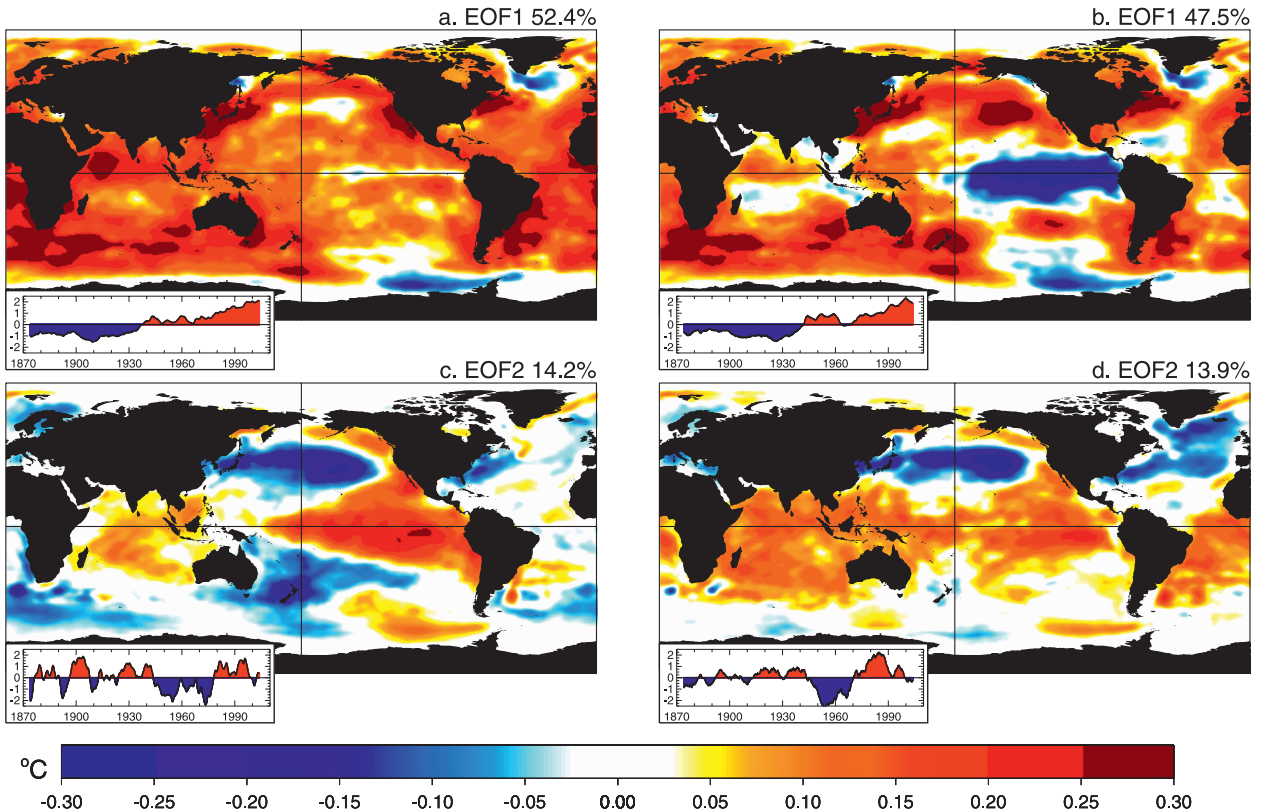
FIG. 10. (left) The two leading EOFs and associated PCs (inset) of 5-yr running mean SST anomalies from the 1871–2006 HadISST dataset and (right) the same quantities computed using the ENSO-unrelated SST anomalies. The fraction of variance explained in (a),(c) the original dataset and (b),(d) the ENSO-unrelated dataset is indicated over each panel. Note that the PCs are normalized to have unit amplitude, while the EOFs show the observed magnitude (°C) for a unit deviation of the PC. The contour interval is 0.05°C.

two leading EOFs and associated PCs of 5-yr running mean HadISST anomalies in the 1871–2006 period. The first EOF of such long-term SST variations is often identified with global warming (Parker et al. 2007). Note that it is similar, but not identical, to the long-term trend pattern in Fig. 8a. The second EOF is often identified with ENSO-like decadal variability (Zhang et al. 1997), a global signature of the Pacific decadal oscillation or the interdecadal Pacific oscillation (Parker et al. 2007). It is strongly reminiscent of the low-frequency tail of ENSO and has, indeed, been argued to be such in previous studies (e.g., Alexander et al. 2002; Newman et al. 2003; Schneider and Cornuelle 2005; Alexander et al. 2008).

The two leading EOFs and associated PCs of the ENSO-unrelated 5-yr running mean SST variations are shown in the right panels of Fig. 10, in the same format as the left panels. The first EOF of these ENSO-unrelated variations is generally very similar to the first EOF of the total variations in Fig. 10a, but not in the tropics. In particular, the eastern Pacific cooling emerges as an important part of this leading pattern, of which there is only a hint in Fig. 10a.

The second EOF of the ENSO-unrelated variations, shown in Fig. 10d, is strongly suggestive of a nearly zonally symmetric multidecadal tropical–extratropical seesaw (TESS). A very similar pattern was identified by Livezey and Smith (1999) as importantly related to North American climate variations, but was interpreted by them as a "global climate change signal" associated with anthropogenic warming. Although the PC time series in Fig. 8d does show a strong "trend" from the 1950s to the 1990s, the multidecadal oscillatory nature of the variation is more obvious in the full record. The tropical aspect of this variation was also identified and interpreted as a tropical "trend" pattern by PM06, but again using a shorter record. As in that study, the PC time series in Fig. 10d has a parabolic shape from the 1950s to the present; however, there is no trend over the full record. These variations appear to be related to the global circulation and precipitation changes, claimed by Baines and Folland (2007) to be associated with an "abrupt climate shift" in the late 1960s, and to changes in Sahel rainfall (see also PM06). A relatively sudden upturn in the late 1960s is also evident in our PC time series in Fig. 10d.

Overall, Fig. 10 shows that one can get quite a different impression of low-frequency SST variations around the globe in the last 136 years after their ENSO-related components are removed. We interpret the ENSO-unrelated variations as representing a combination of anthropogenic, naturally forced, and internally generated coherent multidecadal variations. It is far beyond the scope of this study to attempt a further split into these three component variations. Still, it is tempting to associate EOF-1 of the ENSO-unrelated variability with "forced" and EOF-2 with "natural internal" variability, mainly because PC-1 has a strong long-term trend and PC-2 has no trend. If EOF-2 is, indeed, indicative of a natural multidecadal tropical–extratropical seesaw, then its general upward trend from the 1950s to the 1990s may have been misinterpreted in the climate community as an accelerated "forced" trend and its sharp upturn in the 1960s as an anthropogenic abrupt climate shift. Its relatively large amplitude over the Indian Ocean (compared to EOF-1) suggests that it has played a major role in modulating Indian Ocean SSTs over the last half century, which have also been implicated in several climate change attribution studies (e.g., Hurrell et al. 2004).

### c. SST-based climate indices

SSTs averaged over various large representative areas are widely used as indices of climate variability. The global ocean SST average is one such commonly used measure (Hegerl et al. 2007). As already shown in Fig. 1, removing its ENSO-related component reduces its 136-yr warming trend by 40% from ~0.05 to ~0.03 K decade$^{-1}$. This is also consistent with Angell's (2000) analysis of tropospheric air temperatures, who found that about two-thirds of the overall trend in his data was ENSO unrelated.

The effect of removing ENSO-related components from two other climate indices is illustrated in Fig. 11. The west Pacific/Indian Ocean warm pool encompasses the area of warmest SSTs on the planet. Global mean surface temperature and precipitation are particularly sensitive to SST changes in this area (Barsugli et al. 2006). The black curve in Fig. 11a shows the 10-yr running mean time series of SSTs averaged over the warm pool. Removing its ENSO-related component yields the ENSO-unrelated red curve. It is remarkable that the ENSO-unrelated time series shows a slight cooling trend from ~1900 to the mid-1970s, followed by an abrupt warming and stabilization. The ENSO-related variations have clearly contributed substantially to the observed full time series, contributing a warming influence in the early twentieth century, a cooling influence in the 1980s, and again a warming influence in the early twenty-first century.

Another climate index that has received considerable attention is the index of the Atlantic multidecadal oscillation (AMO) (e.g., Enfield and Mestas-Nuñez 1999; Delworth and Mann 2000), especially for its purported links to Atlantic hurricane variability (Goldenberg et al. 2001), global drought (McCabe and Palecki 2006), and European climate (Parker et al. 2007). It has been suggested that this oscillation may be natural and predictable (Knight et al. 2005). Here we define the AMO index, following Enfield et al. (2001), as the linearly detrended area-averaged North Atlantic SST. Its 10-yr running mean time series is shown as the black curve in Fig. 11b. The multidecadal variations discussed in numerous previous studies are evident and consistent with other datasets and AMO definitions [see Delworth and Mann (2000)]. The version of the AMO index with its ENSO-related components removed is shown as the red curve. It is not aligned precisely with the full index series after about 1990, but is extremely close; to that extent, it confirms that much of the recent increase in detrended North Atlantic SSTs is only weakly ENSO related. In other periods, however, the discrepancy between the black and red curves is indicative of a considerable ENSO influence, such as contributing to an enhancement of the oscillation from ~1900 to the 1950s. Insofar as such ENSO contributions are climate noise, these results suggest that modeling studies of North Atlantic climate variations (e.g., Delworth and Mann 2000; Knight et al. 2005) may have greater success comparing their simulated variations with the ENSO-unrelated variations shown here than with the full observed variations.

## 5. Constancy of ENSO dynamics

The overarching conclusion of this study is that both long-term trends and multidecadal variations over the last 136 years in the Pacific, Indian, and Atlantic Oceans have had substantial ENSO-related components. Because our estimates of these components are somewhat larger than reported in previous studies, and to that extent are also somewhat surprising, it is necessary to reassess some of the assumptions of our analysis. One particular assumption, which we maintain is much weaker than made in other ENSO-removal studies but is nevertheless still an assumption, is that the *dynamics* of ENSO have remained roughly constant over the last 136 years, even if their statistics have not. By this we mean that the ENSO-relevant eigenmode subset of the tropical dynamical evolution operator **L**, shown in Fig. 4, has remained roughly the same in the last 136 years. In the following, we pursue two different lines of evidence in support of this claim; specifically that **L** itself has not shown a systematic trend over the last 136 years.
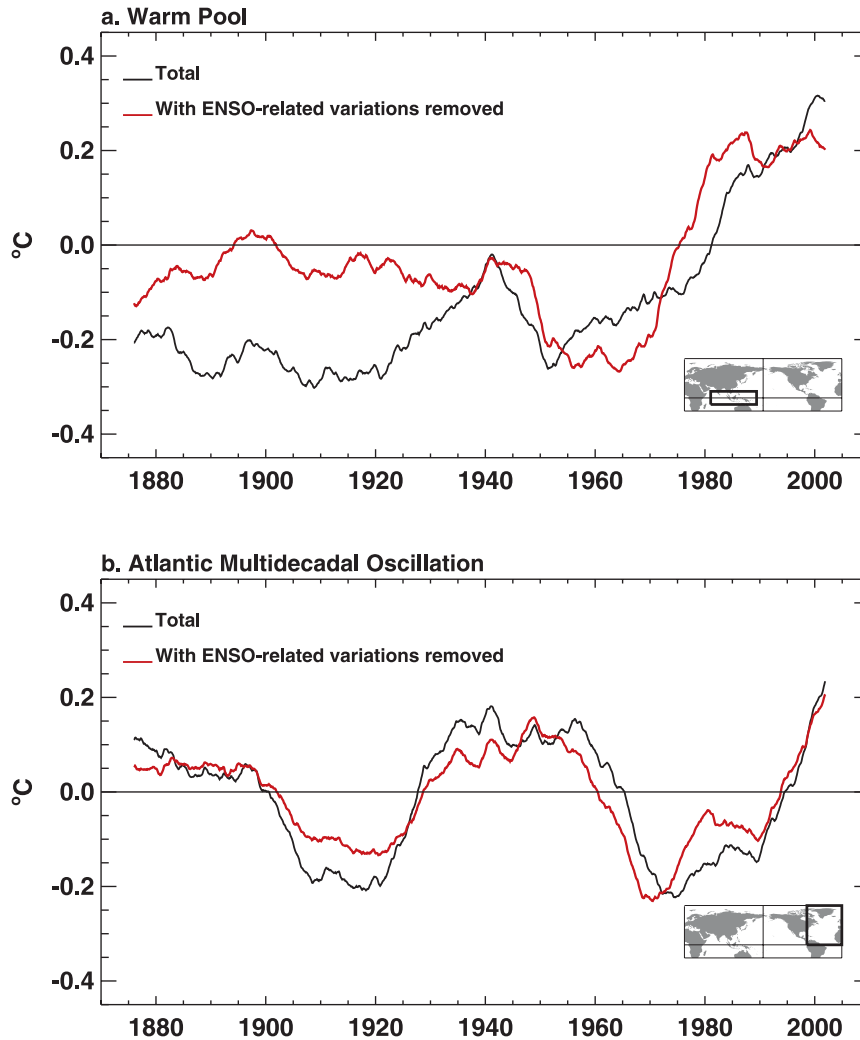
FIG. 11. SST time series of the (a) warm pool and (b) Atlantic multidecadal oscillation (black curves) and their ENSO-unrelated components (red curves). A 10-yr running mean has been applied to all series. Anomalies are relative to the 1949–2004 climatology. Area averages are computed over the regions indicated on the respective inset maps: (a) warm pool (15°N–15°S, 60°–165°E) and (b) AMO (90°N–0°, 80°W–0°).

It has long been thought that one of the most important controlling influences on ENSO dynamics is $\Delta T_{E-W}$, the east–west SST gradient across the tropical Pacific basin (Bjerknes 1969; Neelin et al. 1998 and references therein; Sun 2003). Figure 12 shows that, although $\Delta T_{E-W}$ has varied throughout the record, with 10-yr averaged values of up to 25% larger or smaller than the 1871–2006 average, it has not shown a systematic trend over the entire record. To be sure, there is evidence of an upward "trend" after 1900 (Cane et al. 1997) and in the most recent 50 years (Zhang and McPhaden 2006), but it is clear that they are part of long-term variability with no obvious overall trend.

If the relatively modest long-term variations in $\Delta T_{E-W}$ were important in modulating ENSO variability, one might expect such a modulation to be evident in the variance of ENSO indices such as Niño-3.4 SSTs. The gray shaded curve in Fig. 12 shows the time series of 2–6-yr variance in Niño-3.4 from the HadISST dataset, produced following the method of Torrence and Compo (1998). While there are hints of an association, say during the 1890s and in the most recent decades, there are also periods of large Niño-3.4 variance coexisting with those of weak gradients, such as the early 1900s. These variations of Niño-3.4 variability are consistent with those of other ENSO indices such as Niño-3, the Southern Oscillation index (SOI) (Torrence and Webster 1999), and central Pacific rainfall (Kestin et al. 1998).

It has recently been suggested that the interaction of the subtropical ocean with the equatorial ocean through
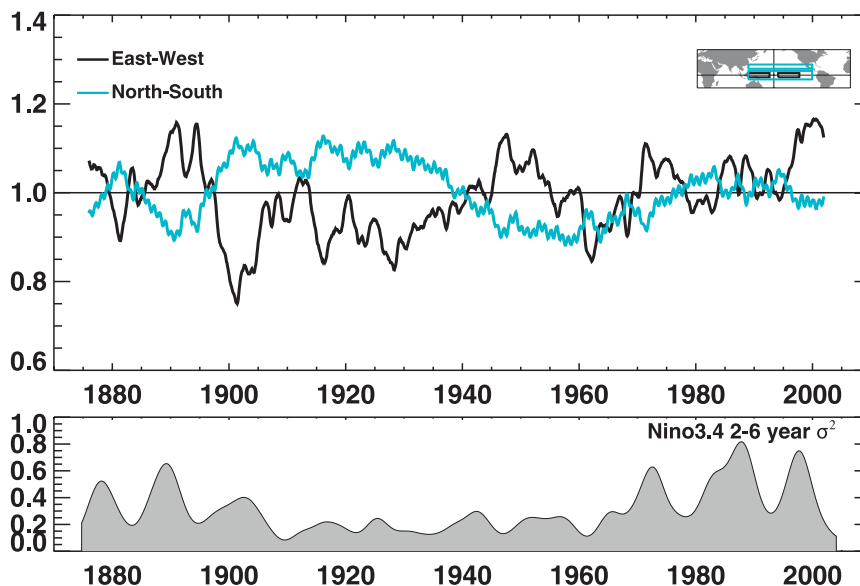
FIG. 12. (top) Time series of east–west and north–south Pacific SST differences scaled by their respective long-term mean values. Black curve: temperature difference between Niño-3.4 and western Pacific warm pool $\Delta T_{E-W}$. The mean difference over 1871–2006 is $-1.98°C$. Blue curve: temperature difference between the north subtropical and tropical Pacific $\Delta T_{N-S}$. The mean difference over 1871–2006 is $-1.74°C$. A 10-yr running average has been applied to the difference series. Regions are shown on the inset map. Black boxes: $\Delta T_{E-W}$ (5°N–5°S, 170°–120°W) minus (5°N–5°S, 120°–170°E); blue boxes: $\Delta T_{N-S}$ (15°N–25°N, 120°E–90°W) minus (10°N–10°S, 120°E–90°W). (bottom) Gray shaded curve: variance of Niño-3.4 SST anomalies in the 2- to 6-yr band determined from wavelet analysis.

"oceanic tunnels" may also be important in modulating ENSO dynamics (e.g., Seager and Murtugudde 1997; Kleeman et al. 1999; Shin and Liu 2000; Sun et al. 2004; Solomon et al. 2008). A simple proxy for this effect is the SST gradient between the north subtropical and tropical Pacific SSTs $\Delta T_{N-S}$. The blue curve in Fig. 12 shows that decadal variations in this gradient have been less than 20% of the long-term mean. Again, there is no obvious correspondence with changes of Niño-3.4 SST variance. Although large changes of $\Delta T_{N-S}$ could be expected to impact ENSO (Collins 2000; Sun et al. 2004), the observed changes have apparently not been large enough in this regard. As such, they have probably not altered the tropical dynamics represented in **L**. They do not appear to be related consistently to variations in the statistics of Niño-3.4 SSTs or to those of other ENSO indices (Wang and Wang 1996; Torrence and Compo 1998; Kestin et al. 1998; Torrence and Webster 1999).

Another way of assessing the near constancy of **L** is to ask to what extent does the forecast skill of the model (4) vary over the 136 years of record if one uses a constant **L** to make the forecasts. Figure 13 shows the 136-yr time series of the pattern correlation of the observed and predicted seasonal tropical SST anomaly fields for various forecast lead times. Recall that the model (i.e., the **L** operator) was developed using the 1949–2004 data at a 3-month lag. Therefore all comparisons for 1871–2006 at 6-month and 12-month lags are independent tests, as is the forecast skill for 1871–1948 at the 3-month lag. The relative constancy of the forecast skill is remarkable. The drop in skill between the 1910s and 1950s may reflect reduced observation availability during the world wars but may also be associated with decreased ENSO variability itself in the period, as reflected in several ENSO indices (Wang and Wang 1996; Torrence and Compo 1998; Kestin et al. 1998; Torrence and Webster 1999) and illustrated for Niño-3.4 SSTs in Fig. 12.

Taken together, the evidence in Figs. 12 and 13 suggests that the tropical ocean dynamics encapsulated in **L** have not changed appreciably in the last 136 years. A similar conclusion was reached by Chen et al. (2004) for the last 150 years using a forward coupled model of intermediate complexity. It is of course true that for sufficiently large changes in the basic state, such as represented in $\Delta T_{E-W}$ or $\Delta T_{N-S}$, one would expect **L** to be sufficiently altered to reduce the advantages of our ENSO-removal method over other methods. So far, however, the basic-state changes appear to have been small enough to justify our linear decomposition throughout the 136-yr period of record.
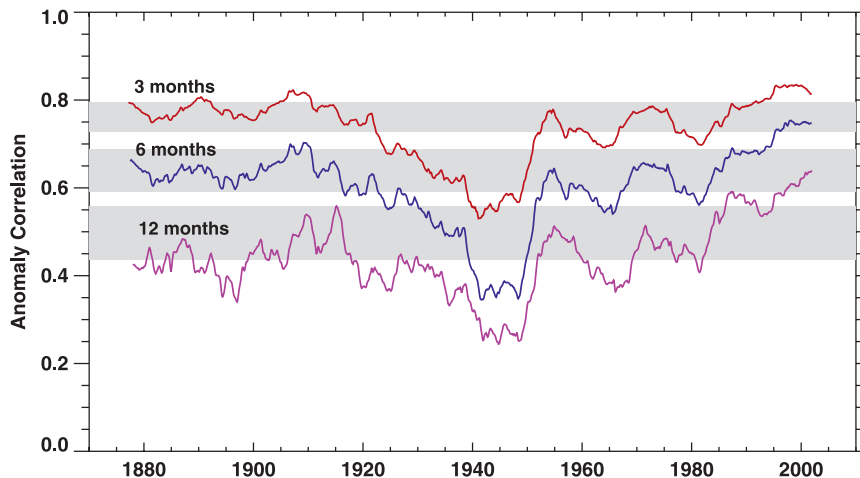
FIG. 13. Time series of the pattern correlation between forecast and observed tropical SST anomaly fields from 1871 to 2006. Forecast skill is shown for leads of 3 months (red curve), 6 months (blue curve), and 12 months (pink curve). A 10-yr running mean has been applied. Gray shading indicates the 95% range of expected fluctuations about the 1949–2004 mean value at each lag.

Given the evidence of the near constancy of **L**, one might wonder if we could have used the entire 136-yr record to construct **L**. We found that we could not have, owing to sparse observations in key regions in the early part of the record. For example, we estimated **L** using the 1872–1947 data. The optimal final structure $\psi_1$ using these data had a pattern correlation with the $\psi_1$ in Fig. 3b of 0.95. However, $\phi_1$, the optimal initial structure, had a pattern correlation with the $\phi_1$ in Fig. 3a of only 0.25. One could have anticipated this result after considering the data availability in regions in which these structures have large amplitude (Fig. 14). Figure 14a shows the number of SST observations in the International Comprehensive Ocean–Atmosphere Data Set (ICOADS) collection (Worley et al. 2005), which represents a superset of that used to construct the HadISST fields, in March through May in two regions where $\phi_1$ has large amplitude. The data availability in March–May is relevant since this is when most ENSO events emerge (PS95; Harrison and Larkin 1998). There were clearly far fewer observations in these months in these key regions in the late nineteenth and early twentieth centuries. In contrast, the central equatorial Pacific region of large amplitude of $\psi_1$ was well observed in the mature December–February phase of ENSO throughout the record (Fig. 14b). It was in recognition of such constraints on data availability that we decided to estimate **L** using the more recent 1949–2004 period in which there were sufficient observations to determine both $\phi_1$ and $\psi_1$ with sufficient accuracy.

## 6. Summary and conclusions

In this paper, we have argued that identifying and removing ENSO-related variations by performing regressions on any single ENSO index can be problematic. We stressed that ENSO is best viewed not as a *number* but as an evolving *dynamical process* for this purpose. Specifically, we identified ENSO with those four dynamical eigenvectors of tropical SST evolution that are most important in the observed evolution of ENSO events over several seasons. We used this definition to isolate the ENSO-related component of global SST variations on a month-by-month basis in the 136-yr (1871–2006) HadISST dataset.

We find that removing ENSO-related variations has a large effect on long-term SST trends and on the dominant patterns of low-frequency (5-yr running mean) SST variability. We interpret the low-frequency ENSO-unrelated SST variations as reflecting an as yet undetermined combination of anthropogenic, naturally forced, and coherent internal multidecadal variations. The first EOF of the ENSO-unrelated data has a general global warming structure, but also a pronounced *cooling* in the eastern equatorial Pacific, which, although surprising, is not unphysical. The second EOF is strongly suggestive of a multidecadal zonally symmetric tropical–extratropical SST seesaw pattern. It is not clear to what extent it reflects a pattern of forced or natural variability. We are more inclined toward interpreting it as the latter, given that the amplitude time series of this pattern has no trend over the last 136 years.
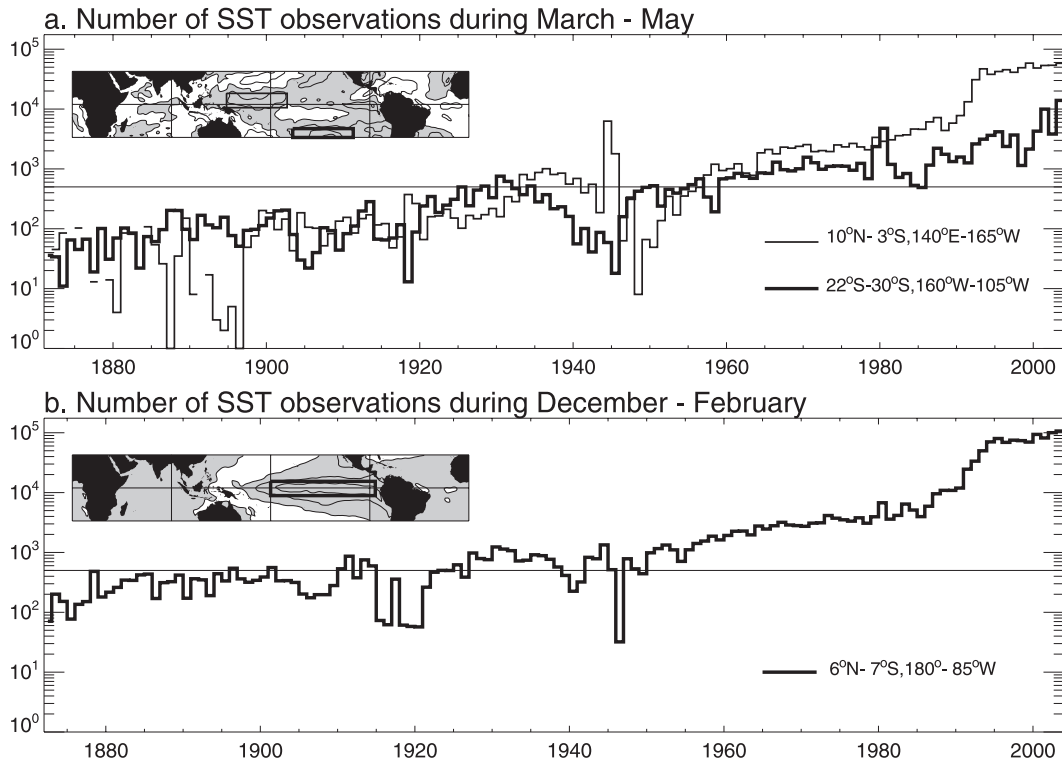
FIG. 14. Time series of the number of SST observations available in the ICOADS collection for selected seasons and regions from 1871 to 2006. (a) During March through May in two regions of large loading of the optimal initial structure [see inset (10°–3°N, 140°E–165°W); (22°–30°S, 160°–105°W)]. (b) During December through February in the region of large loading of the optimal evolved structure [see inset (6°N–7°S, 85°W–180°)]. The number of observations is shown on a logarithmic scale. The thin line in both panels indicates 500 SST observations per season.

It is important to recognize that our decomposition of the low-frequency SST fields into ENSO-unrelated and ENSO-related parts is not strictly the same as into "predictable" and "unpredictable" parts. The ENSO-unrelated parts may be predictable if the relevant anthropogenic and natural radiative forcings are predictable and the appropriate initial conditions for coherent internal long-term variations are known. The ENSO-related parts, as identified by us, include both the unpredictable low-frequency tail of ENSO and the potentially predictable projection of anthropogenic and naturally forced SST variations on the eight ENSO mode patterns in Fig. 4. In other words, our ENSO-unrelated low-frequency fields may be mostly predictable, but our ENSO-related fields may not be totally unpredictable. (Nonetheless, we suspect that any such ENSO-related low-frequency predictability was small in our period of interest, as there is no obvious trend in any of the ENSO modal time series in Fig. 5 that one could immediately attribute to an anthropogenically forced or naturally forced response.) This comment applies equally, of course, to any other pattern-based method, including all EOF-based methods, of identifying ENSO-related climate variations.

These issues are schematically illustrated in Fig. 15. Each circular ring, representing the totality of any particular climate variation (e.g., a 50-yr trend field), is divided into two segments depending on the type of decomposition employed. Three types of decompositions are considered. With regard to a 50-yr trend field, for instance, they would represent decompositions of the field into anthropogenic and natural, predictable and unpredictable, and ENSO-unrelated and ENSO-related components. The important point illustrated in Fig. 15 is that, although it is tempting to think so, such decompositions are in general not strictly congruent. In other words, anthropogenic ≠ predictable ≠ ENSO unrelated, and natural ≠ unpredictable ≠ ENSO related, in the strictest sense. (For example, if an anthropogenic climate trend pattern has a large projection in the space of the ENSO modes shown in Fig. 4, then that projected trend component will also contribute to the ENSO-related trend obtained by our method. The nearly zero long-term trend in the time series of the ENSO modes shown in Fig. 5 suggests, however, that such contributions were small over the twentieth century.) This noncongruence is indicated in Fig. 15 by the overlap at the segment
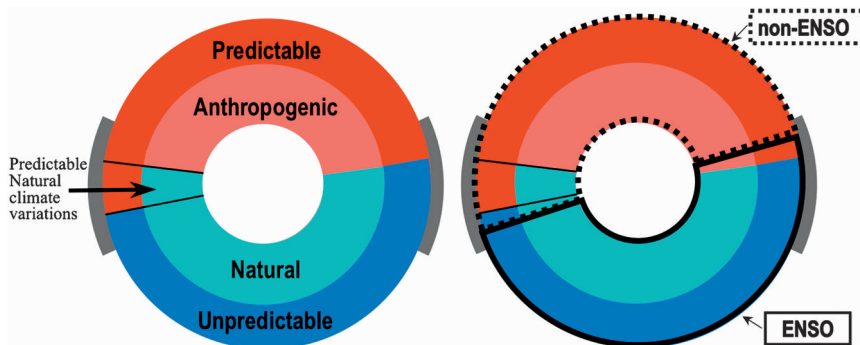
FIG. 15. (left) Circular rings schematically illustrate the totality of any particular climate variation (e.g., a 50-yr trend). Each ring is divided into two segments depending on the decomposition used. Two types of decompositions are predictable and unpredictable (outer red and blue ring) and anthropogenic and natural (inner red and blue ring). The gray arcs overlapping the segment boundaries illustrate that these decompositions are not necessarily congruent; e.g., some natural climate variations may be predictable. (right) The relationships between a third, ENSO/non-ENSO decomposition (solid black and perforated ring) and the other two decompositions are illustrated. For clarity, the labels are not repeated from the left panel. The three rings illustrate how, e.g., the non-ENSO component may be generally identified with the anthropogenic and predictable components of climate variations but with the gray arcs again emphasizing that the congruence is not exact.

boundaries. Such overlaps complicate climate diagnosis, but they are real and arise from the physically based nonorthogonality of the component variations in both the spatial and temporal domains. Assuming orthogonality in either of these domains for diagnostic expediency can lead to wrong conclusions. An example of spatial nonorthogonality, with regard to ENSO, is that the anthropogenic signal in global temperature is not spatially orthogonal to the global ENSO signal; after all, 1998 remains the warmest year of the instrumental record since 1850, according to Brohan et al. (2006). As is already well accepted, ENSO plays a role in global mean temperature variations (e.g., Robock and Mao 1995; Kelly and Jones 1996; Angell 2000; Thompson et al. 2008, 2009). Therefore, any definition of ENSO must account for the global mean part of the phenomenon. An example of temporal nonorthogonality, again with regard to ENSO, is that ENSO is not a frequency-band-limited phenomenon and clearly has a low-frequency tail, so any definition of ENSO must account for that low-frequency tail, as stressed repeatedly in this paper.

Our demonstration that ENSO-related trend components account for a substantial part of twentieth-century SST trends provides strong motivation for accurately representing the ENSO eigenmodes documented here in climate models, regardless of the relative magnitudes of the unpredictable noise and potentially predictable anthropogenic contributions to those ENSO-related trends. This is because, on the one hand, the very existence of unpredictable trend components associated with the low-frequency tail of ENSO necessitates an accurate

representation of ENSO dynamics and ENSO-related climate variability that, even if it is just noise, can strongly affect multidecadal and longer-term climate variations around the globe. On the other hand, a substantial future anthropogenic forcing of the ENSO eigenmodes would affect not only ENSO dynamics but also the spatial pattern of the tropical SST change, with important implications for global climate change (Barsugli et al. 2006).

## APPENDIX A

### Details of Linear Inverse Model implementation

As discussed in PS95, a consistency requirement for the validity of (3) and (4) is that the estimate of **L** be

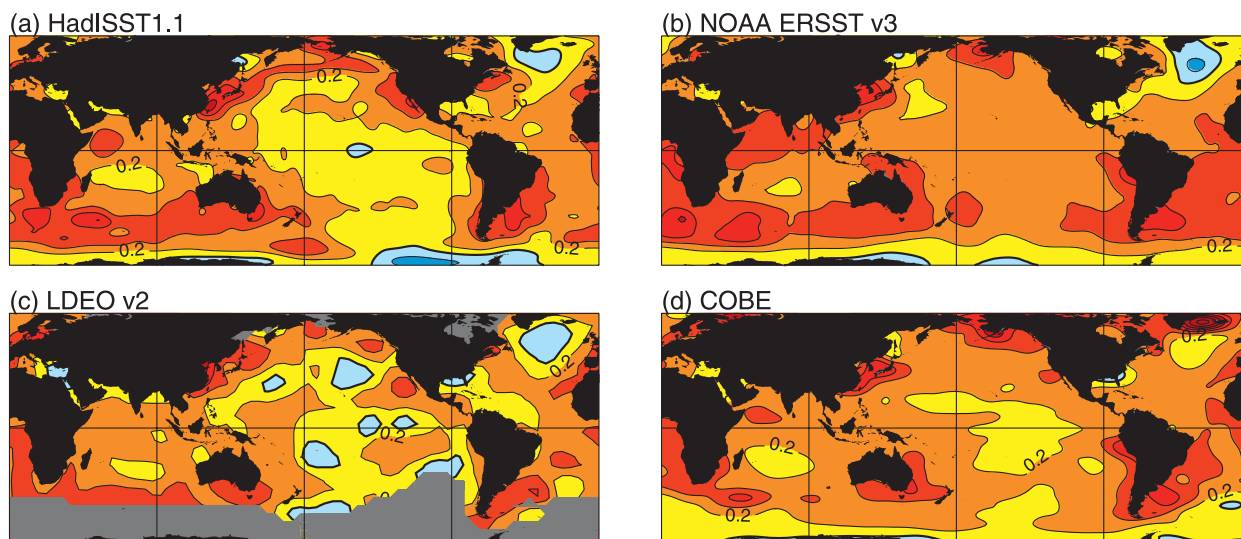## Observed Trend of Global SSTs in Four Data Sets (1901-2005) °C/50 yr



FIG. C1. Global maps of linear trends over 1901–2005 from four different SST datasets: (a) HadISST v1.1, (b) NOAA ERSST version 3, (c) LDEO SST version 2, and (d) COBE SST. Contour interval is 0.2°C change per 50 years. The zero contour is thickened.

independent of the particular choice of $\tau_o$. In this study, we used $\tau_o = 3$ months as in PM06 and the 1949–2004 monthly HadISST SST data to estimate the $\mathbf{C}(0)$ and $\mathbf{C}(\tau_o)$ matrices. The choice of the second half of the HadISST dataset for this purpose was partly motivated by the fact that 1949 marks a significant increase in the input data density used in constructing the dataset (Rayner et al. 2003) and partly by a need to leave an "independent" first half for assessing the dynamical stationarity of $\mathbf{L}$. As in PM06, $\mathbf{L}$ was estimated using SSTs in the entire tropical domain 30°N–30°S. Penland and Matrosova (1998) show that the LIM results obtained using this domain are similar to those obtained using a more limited Indo-Pacific domain. Three-month running mean anomalies were formed at each grid point as differences from the 1949–2004 monthly average annual cycle. The 1° data were spatially smoothed using a 3° latitude, 5° longitude boxcar smoother. These smoothed fields were then projected on a truncated space of 20 SST EOF patterns, retaining about 89% of the SST variance. The time varying coefficients of these 20 EOFs, that is, the 20 PC time series, define the truncated 20-component tropical SST vector $\mathbf{x}(t)$ used for isolating $\mathbf{x}_e(t)$ in this study.

Extensive sensitivity and cross-validation exercises were performed for all EOF truncations from 2 to 30 before settling on the choice of 20 EOFs, using the skill of tropical SST hindcasts based on (4) as a guiding criterion. This was done by excluding, in turn, each of eight contiguous 7-yr segments from the data, estimating $\mathbf{L}$

from the remaining 49 years, and then performing hindcasts in the excluded 7-yr segment. The best average hindcast skill was obtained for a 20-EOF truncation, in terms of both anomaly pattern correlation skill and rms error over the domain.

## APPENDIX B

### Objective Selection of ENSO-Related Eigenmodes

We determined the ENSO-relevant subset $\{\mathbf{U}_k\}$ of the eigenvectors of $\mathbf{L}$ objectively as follows. First, we imposed a time-scale constraint consistent with the 18–24-month upper bound on ENSO predictability found in previous studies (e.g., PS95; Chen et al. 2004). Modes with a decay time scale of longer than 24 months cannot contribute to predictable ENSO evolution, otherwise ENSO predictability would extend beyond 24 months. We therefore excluded modes with a longer decay time scale. Using the shorter 18-month limit of PS95 did not affect the result since this criterion excludes only one eigenmode of $\mathbf{L}$, a purely decaying mode with a decay time scale of ~40 months. A similar mode was also excluded by PM06. The remaining modes were ranked by the magnitude of the inner product of their corresponding adjoint eigenvector $\mathbf{V}_k$ (i.e., the eigenvector of $\mathbf{L}^T$ with the same eigenvalue) with $\boldsymbol{\phi}_1$. Then, starting with the mode having the largest inner product and longest effective time scale, a truncated $\mathbf{G}$ (8) operator was constructed

TABLE C1. Pattern correlations between four observational SST datasets of 1901–2005 SST trend from 60°N to 60°S with (and also without) the area mean included.

| | HadISST | NOAA ERSSTv3 | LDEO | COBE |
|---|---|---|---|---|
| HadISST | 1 | 0.91 (0.59) | 0.89 (0.63) | 0.91 (0.64) |
| NOAA ERSSTv3 | | 1 | 0.89 (0.53) | 0.93 (0.54) |
| LDEO | | | 1 | 0.89 (0.57) |
| COBE | | | | 1 |

using only this eigenmode. Its dominant right and left singular vectors and singular value were compared with the $\phi_1, \psi_1$, and $\gamma_1$ obtained from the full **G** (8) operator. If the pattern correlations exceeded 0.5, the mode was included in the ENSO-relevant subset; if not, the procedure was repeated for succeeding modes in the ranked list until they did. The criterion for including additional modes in the subset was whether their inclusion improved the approximation to $\phi_1, \psi_1$, and $\gamma_1$. A mode was included if the pattern correlations with $\phi_1$ and $\psi_1$ increased, and the singular value also increased, or decreased by less than 5% of $\gamma_1$. Applying this procedure yielded a total of four ENSO-relevant eigenmodes (Fig. 4). Remarkably, we found this selection algorithm to be completely insensitive to the order of consideration of the subsequent modes when the threshold pattern correlation for selection of the first member of the subset was set at 0.5 or higher.

## APPENDIX C

## Comparison of SST Trends Using Different SST Datasets

Global SST trends for 1901–2005 computed using four different datasets are shown in Fig. C1. The period was chosen to facilitate comparison with similar trends contained in the Intergovernmental Panel on Climate Change (IPCC) Fourth Assessment report (Hegerl et al. 2007; Trenberth et al. 2007). Least squares linear trends were computed using the HadISST1.1 dataset, National Oceanic and Atmospheric Administration (NOAA) Extended Reconstructed SST (ERSSTv3) (Smith et al. 2008), Lamont Doherty Earth Observatory SST (LDEOv2) (Kaplan et al. 1998), and Centennial in Situ Observation Based Estimates of SST (COBE) (Ishii et al. 2005). The datasets differ in their input SST observations and methods of interpolation. Unlike the HadISST, ERSST, and LDEO datasets, the COBE optimal interpolation dataset does not employ an EOF basis (Ishii et al. 2005; M. Ishii 2009, personal communication). Instead, COBE uses a variational scheme with prespecified optimal analysis parameters. Comparing the four datasets, we see that the trends are generally similar (Table C1), with apparent discrepancies in the equatorial Pacific (see also Vecchi and Soden 2007), western Indian Ocean, North Pacific, and south of Greenland (Fig. C1). The two datasets that make no assumption about the spatiotemporal structure of low-frequency variability (LDEO and

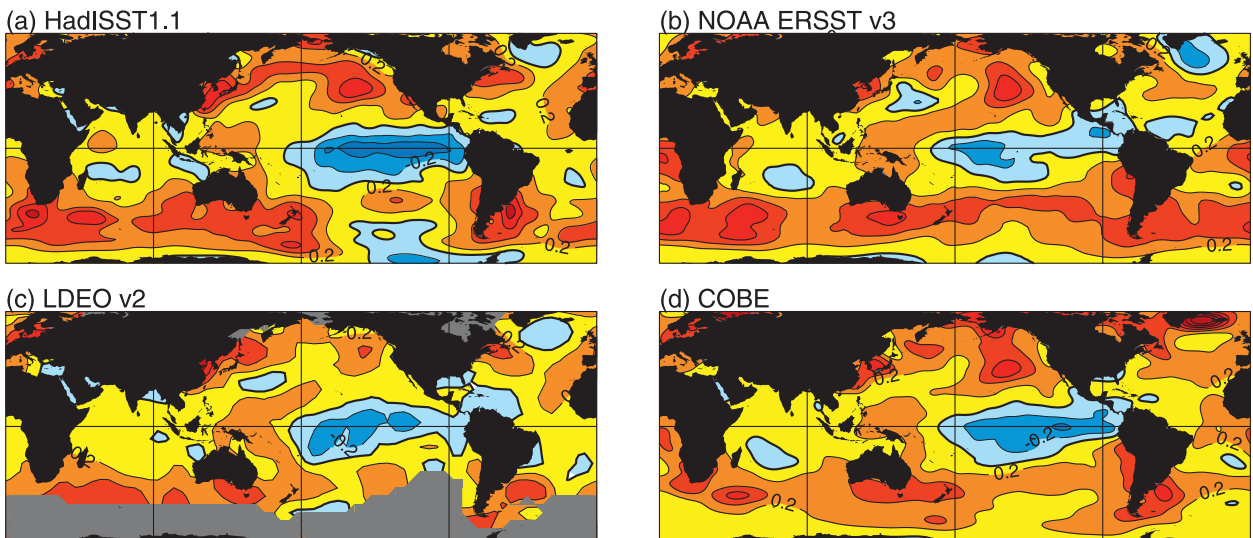ENSO-unrelated Trend of Global SSTs in Four Data Sets (1901-2005) °C/50 yr



FIG. C2. As in Fig. C1 but for ENSO-unrelated trends.

TABLE C2. As in Table C1 but for pattern correlations between ENSO-unrelated SST datasets of 1901–2005 SST trend from 60°N to 60°S with (and also without) the area mean included.

| | HadISST | NOAA ERSSTv3 | LDEO | COBE |
|---|---|---|---|---|
| HadISST | 1 | 0.82 (0.72) | 0.83 (0.76) | 0.89 (0.83) |
| NOAA ERSSTv3 | | 1 | 0.79 (0.67) | 0.87 (0.76) |
| LDEO | | | 1 | 0.83 (0.74) |
| COBE | | | | 1 |

COBE, Figs. C1c and C1d) appear to agree more closely with the spatial variations of the HadISST trend map than does the NOAA ERSSTv3b (Table C1), particularly in the eastern equatorial Pacific trend representing a relative minimum compared to the rest of the tropics. A comprehensive comparison of these datasets, including their trends and variability, is beyond the scope of the present study. Other researchers (M. Newman 2009, personal communication) and the Global Climate Observing System Working Group on Sea Surface Temperature and Sea Ice (T. Brandon 2009, personal communication) are undertaking such an investigation.

Our EPF from Eq. (10) has been applied to all four datasets to form an estimate of the ENSO-unrelated trend (Fig. C2). It is remarkable that, despite the use of a different ENSO-removal technique and 15 additional years of data, we obtain nearly the same ENSO-unrelated trend as found by Cane et al. (1997), as evident from a comparison of Fig. C2c with their Fig. 3b (not shown here). In general, the ENSO-unrelated trend patterns from all four datasets are broadly similar (Table C2). In particular, all four show that the long-term ENSO-unrelated trend in the eastern equatorial Pacific is one of cooling. This regional cooling trend is also evident in trends over other periods (as in Figs. 8 and 9) and in previous studies (Cane et al. 1997; Lau and Weng 1999; Guan and Nigam 2008).

## REFERENCES

Alexander, M. A., I. Bladé, M. Newman, J. R. Lanzante, N.-C. Lau, and J. D. Scott, 2002: The atmospheric bridge: The influence of ENSO teleconnections on air–sea interaction over the global oceans. *J. Climate,* **15,** 2205–2231.

——, L. Matrosova, C. Penland, J. D. Scott, and P. Chang, 2008: Forecasting Pacific SSTs: Linear inverse model predictions of the PDO. *J. Climate,* **21,** 385–402.

Angell, J. K., 2000: Tropospheric temperature variations adjusted for El Niño, 1958–1998. *J. Geophys. Res.,* **105** (D9), 11 841–11 849.

Baines, P. G., and C. K. Folland, 2007: Evidence for a rapid global climate shift across the late 1960s. *J. Climate,* **20,** 2721–2744.

Barsugli, J. J., S.-K. Shin, and P. D. Sardeshmukh, 2006: Sensitivity of global warming to the pattern of tropical ocean warming. *Climate Dyn.,* **27,** 483–492, doi:10.1007/s00382-006-0143-7.

Bjerknes, J., 1969: Atmospheric teleconnections from the equatorial Pacific. *Mon. Wea. Rev.,* **97,** 163–172.

Borges, M. A., and P. D. Sardeshmukh, 1995: Barotropic Rossby wave dynamics of zonally varying upper-level flows during northern winter. *J. Atmos. Sci.,* **52,** 3779–3796.

Brohan, P., J. J. Kennedy, I. Harris, S. F. B. Tett, and P. D. Jones, 2006: Uncertainty estimates in regional and global observed temperature changes: A new data set from 1850. *J. Geophys. Res.,* **111,** D12106, doi:10.1029/2005JD006548.

Cane, M. A., A. C. Clement, A. Kaplan, Y. Kushnir, D. Pozdnyakov, R. Seager, S. E. Zebiak, and R. Murtugudde, 1997: Twentieth-century sea surface temperature trends. *Science,* **275,** 957–960.

Chen, D., M. A. Cane, A. Kaplan, S. E. Zebiak, and D. Huang, 2004: Predictability of El Niño over the past 148 years. *Nature,* **428,** 733–736.

Chiang, J. C. H., and D. J. Vimont, 2004: Analogous Pacific and Atlantic meridional modes of tropical atmosphere–ocean variability. *J. Climate,* **17,** 4143–4158.

Clement, A. C., R. Seager, M. A. Cane, and S. E. Zebiak, 1996: An ocean dynamical thermostat. *J. Climate,* **9,** 2190–2196.

Collins, M., 2000: Understanding uncertainties in the response of ENSO to greenhouse warming. *Geophys. Res. Lett.,* **27,** 3509–3512.

Covey, D. L., and S. Hastenrath, 1978: The Pacific El Niño phenomenon and the Atlantic circulation. *Mon. Wea. Rev.,* **106,** 1280–1287.

Delworth, T. L., and M. E. Mann, 2000: Observed and simulated multidecadal variability in the Northern Hemisphere. *Climate Dyn.,* **16,** 661–676.

Enfield, D. B., and A. M. Mestas-Nuñez, 1999: Multiscale variabilities in global sea surface temperatures and their relationships with tropospheric climate patterns. *J. Climate,* **12,** 2719–2733.

——, ——, and P. J. Trimble, 2001: The Atlantic multidecadal oscillation and its relation to rainfall and river flows in the continental U.S. *Geophys. Res. Lett.,* **28,** 2077–2080.

Folland, C. K., D. E. Parker, A. W. Coleman, and R. Washington, 1999: Large scale modes of ocean surface temperature since the late nineteenth century. *Beyond El Niño: Decadal and Interdecadal Climate Variability,* A. Navarra, Ed., Springer-Verlag, 73–102.

Fu, C., H. F. Diaz, and J. O. Fletcher, 1986: Characteristics of the response of sea surface temperature in the central Pacific associated with warm episodes of the Southern Oscillation. *Mon. Wea. Rev.,* **114,** 1716–1738.

Garcia, A., and C. Penland, 1991: Fluctuating hydrodynamics and principal oscillation pattern analysis. *J. Stat. Phys.,* **64,** 1121–1132.

Goldenberg, S. B., C. W. Landsea, A. M. Mestas-Nuñez, and W. M. Gray, 2001: The recent increase in Atlantic hurricane activity: Causes and implications. *Science,* **293,** 474–479.

Guan, B., and S. Nigam, 2008: Pacific sea surface temperatures in the twentieth century: An evolution-centric analysis of variability and trend. *J. Climate,* **21,** 2790–2809.

Hansen, J., M. Sato, R. Ruedy, K. Lo, D. W. Lea, and M. Medina-Elizade, 2006: Global temperature change. *Proc. Natl. Acad. Sci. USA,* **103,** 14 288–14 293.

Harrison, D. E., and N. K. Larkin, 1998: El Niño-Southern Oscillation sea surface temperature and wind anomalies, 1946-1993. *Rev. Geophys.,* **36,** 353–399.

Hegerl, G. C., and Coauthors, 2007: Understanding and attributing climate change. *Climate Change 2007: The Physical Science Basis,* S. Solomon et al., Eds., Cambridge University Press, 663–746.

Hurrell, J. W., M. P. Hoerling, A. S. Phillips, and T. Xu, 2004: Twentieth century North Atlantic climate change. Part I: Assessing determinism. *Climate Dyn.,* **23,** 371–389, doi:10.1007/s00382-004-0432-y.

Ishii, M., A. Shouji, S. Sugimoto, and T. Matsumoto, 2005: Objective analyses of sea-surface temperature and marine meteorological variables for the 20th century using ICOADS and the KOBE collection. *Int. J. Climatol.,* **25,** 865–879.

Joseph, R., and S. Nigam, 2006: ENSO evolution and teleconnections in IPCC's twentieth-century climate simulations: Realistic representation? *J. Climate,* **19,** 4360–4377.

Kaplan, A., M. A. Cane, Y. Kushnir, A. C. Clement, M. B. Blumenthal, and B. Rajagopalan, 1998: Analyses of global sea surface temperature 1856–1991. *J. Geophys. Res.,* **103** (C9), 18 567–18 589.

Karnauskas, K. B., R. Seager, A. Kaplan, Y. Kushnir, and M. A. Cane, 2009: Observed strengthening of the zonal sea surface temperature gradient across the equatorial Pacific Ocean. *J. Climate,* **22,** 4316–4321.

Kelly, P. M., and P. D. Jones, 1996: Removal of the El Niño–Southern Oscillation signal from the gridded surface air temperature data set. *J. Geophys. Res.,* **101** (D14), 19 013–19 022.

Kestin, T. S., D. J. Karoly, J. I. Yano, and N. A. Rayner, 1998: Time–frequency variability of ENSO and stochastic simulations. *J. Climate,* **11,** 2258–2272.

Kleeman, R., J. P. McCreary, and B. A. Klinger, 1999: A mechanism for generating ENSO decadal variability. *Geophys. Res. Lett.,* **26,** 1743–1746.

Knight, J. R., R. J. Allan, C. K. Folland, M. Vellinga, and M. E. Mann, 2005: A signature of persistent natural thermohaline circulation cycles in observed climate. *Geophys. Res. Lett.,* **32,** L20708, doi:10.1029/2005GL024233.

Knutson, T. R., and Coauthors, 2006: Assessment of twentieth-century regional surface temperature trends using the GFDL CM2 coupled models. *J. Climate,* **19,** 1624–1651.

Kumar, A., and M. P. Hoerling, 2003: The nature and causes for the delayed atmospheric response to El Niño. *J. Climate,* **16,** 1391–1403.

Lanzante, J. R., 1996: Lag relationships involving tropical sea surface temperatures. *J. Climate,* **9,** 2568–2578.

Lau, K.-M., and H. Weng, 1999: Interannual, decadal–interdecadal, and global warming signals in sea surface temperature during 1955–97. *J. Climate,* **12,** 1257–1267.

Livezey, R. E., and T. M. Smith, 1999: Covariability of aspects of North American climate with global sea surface temperatures on interannual to interdecadal timescales. *J. Climate,* **12,** 289–302.

McCabe, G. J., and M. A. Palecki, 2006: Multidecadal climate variability of global lands and oceans. *Int. J. Climatol.,* **26,** 849–865.

Meehl, G. A., and Coauthors, 2007: Global climate projections. *Climate Change 2007: The Physical Science Basis,* S. Solomon et al., Eds., Cambridge University Press, 747–846.

Moore, A. M., and R. Kleeman, 1999: The nonnormal nature of El Niño and intraseasonal variability. *J. Climate,* **12,** 2965–2982.

Moron, V., R. Vautard, and M. Ghil, 1998: Trends, interdecadal and interannual oscillations in global sea-surface temperature. *Climate Dyn.,* **14,** 545–569.

Neelin, J. D., D. S. Battisti, A. C. Hirst, F.-F. Jin, Y. Wakata, T. Yamagata, and S. E. Zebiak, 1998: ENSO theory. *J. Geophys. Res.,* **103** (C7), 14 261–14 290.

Newman, M., and P. D. Sardeshmukh, 1998: The impact of the annual cycle on the North Pacific/North American response to remote low-frequency forcing. *J. Atmos. Sci.,* **55,** 1336–1353.

——, G. P. Compo, and M. A. Alexander, 2003: ENSO-forced variability of the Pacific decadal oscillation. *J. Climate,* **16,** 3853–3857.

——, P. D. Sardeshmukh, and C. Penland, 2009: How important is air–sea coupling in ENSO and MJO evolution? *J. Climate,* **22,** 2958–2977.

Parker, D., C. Folland, A. Scaife, J. Knight, A. Colman, P. Baines, and B. Dong, 2007: Decadal to multidecadal variability and the climate change background. *J. Geophys. Res.,* **112,** D18115, doi:10.1029/2007JD008411.

Penland, C., and T. Magorian, 1993: Prediction of Niño 3 sea surface temperatures using linear inverse modeling. *J. Climate,* **6,** 1067–1076.

——, and P. D. Sardeshmukh, 1995: The optimal growth of tropical sea surface temperature anomalies. *J. Climate,* **8,** 1999–2024.

——, and L. Matrosova, 1998: Prediction of tropical Atlantic sea surface temperatures using linear inverse modeling. *J. Climate,* **11,** 483–496.

——, and ——, 2006: Studies of El Niño and interdecadal variability in tropical sea surface temperatures using a nonnormal filter. *J. Climate,* **19,** 5796–5815.

Rayner, N. A., D. E. Parker, E. B. Horton, C. K. Folland, L. V. Alexander, D. P. Rowell, E. C. Kent, and A. Kaplan, 2003: Global analyses of sea surface temperature, sea ice, and night marine air temperatures since the late nineteenth century. *J. Geophys. Res.,* **108,** 4407, doi:10.1029/2002JD002670.

Robock, A., and J. Mao, 1995: The volcanic signal in surface temperature observations. *J. Climate,* **8,** 1086–1103.

Schneider, N., and B. D. Cornuelle, 2005: The forcing of the Pacific decadal oscillation. *J. Climate,* **18,** 4355–4373.

Seager, R., and R. Murtugudde, 1997: Ocean dynamics, thermocline adjustment, and regulation of tropical SST. *J. Climate,* **10,** 521–534.

Shin, S.-I., and Z. Liu, 2000: Response of the equatorial thermocline to extratropical buoyancy forcing. *J. Phys. Oceanogr.,* **30,** 2883–2905.

Smith, T. M., R. W. Reynolds, T. C. Peterson, and J. Lawrimore, 2008: Improvements to NOAA's historical Merged Land–Ocean Surface Temperature Analysis (1880–2006). *J. Climate,* **21,** 2283–2296.

Solomon, A., S.-I. Shin, M. A. Alexander, and J. P. McCreary, 2008: The relative importance of tropical variability forced from the North Pacific through ocean pathways. *Climate Dyn.,* **31,** 315–331, doi:10.1007/s00382-007-0353-7.

Sun, D.-Z., 2003: A possible effect of an increase in the warm pool SST on the magnitude of El Niño warming. *J. Climate,* **16,** 185–205.

——, T. Zhang, and S.-I. Shin, 2004: The effect of subtropical cooling on the amplitude of ENSO: A numerical study. *J. Climate,* **17,** 3786–3798.

Sweeney, C., A. Gnanadesikan, S. M. Griffies, M. J. Harrison, A. J. Rosati, and B. L. Samuels, 2005: Impacts of shortwave penetration depth on large-scale ocean circulation and heat transport. *J. Phys. Oceanogr.,* **35,** 1103–1119.

Thompson, C. J., and D. S. Battisti, 2000: A linear stochastic dynamical model of ENSO. Part I: Model development. *J. Climate,* **13,** 2818–2832.

Thompson, D. W. J., J. J. Kennedy, J. M. Wallace, and P. D. Jones, 2008: A large discontinuity in the mid-twentieth century in observed global-mean surface temperature. *Nature,* **453,** 646–649.

——, J. M. Wallace, P. D. Jones, and J. J. Kennedy, 2009: Identifying signatures of natural climate variability in time series of

global-mean surface temperature: Methodology and insights. *J. Climate,* **22,** 6120–6141.

Torrence, C., and G. P. Compo, 1998: A practical guide to wavelet analysis. *Bull. Amer. Meteor. Soc.,* **79,** 61–78.

——, and P. J. Webster, 1999: Interdecadal changes in the ENSO–monsoon system. *J. Climate,* **12,** 2679–2690.

Trenberth, K. E., and L. Smith, 2006: The vertical structure of temperature in the tropics: Different flavors of El Niño. *J. Climate,* **19,** 4956–4973.

——, and Coauthors, 2007: Observations: Surface and atmospheric climate change. *Climate Change 2007: The Physical Science Basis,* S. Solomon et al., Eds., Cambridge University Press, 235–336.

Vecchi, G. A., and B. J. Soden, 2007: Global warming and the weakening of the tropical circulation. *J. Climate,* **20,** 4316–4340.

Vimont, D. J., 2005: The contribution of the interannual ENSO cycle to the spatial pattern of decadal ENSO-like variability. *J. Climate,* **18,** 2080–2092.

Vyushin, D., and P. J. Kushner, 2009: Power-law and long-memory characteristics of the atmospheric general circulation. *J. Climate,* **22,** 2890–2904.

Wallace, J. M., E. M. Rasmusson, T. P. Mitchell, V. E. Kousky, E. S. Sarachik, and H. von Storch, 1998: On the structure and evolution of ENSO-related climate variability in the tropical Pacific: Lessons from TOGA. *J. Geophys. Res.,* **103** (C7), 14 241–14 269.

Wang, B., and Y. Wang, 1996: Temporal structure of the Southern Oscillation as revealed by waveform and wavelet analysis. *J. Climate,* **9,** 1586–1598.

Wheeler, M. C., and H. H. Hendon, 2004: An all-season real-time multivariate MJO index: Development of an index for monitoring and prediction. *Mon. Wea. Rev.,* **132,** 1917–1932.

Worley, S. J., S. D. Woodruff, R. W. Reynolds, S. J. Lubker, and N. Lott, 2005: ICOADS release 2.1 data and products. *Int. J. Climatol.,* **25,** 823–842.

Zhang, D., and M. J. McPhaden, 2006: Decadal variability of the shallow Pacific meridional overturning circulation: Relation to tropical sea surface temperatures in observations and climate change models. *Ocean Modell.,* **15,** 250–273.

Zhang, Y., J. M. Wallace, and D. S. Battisti, 1997: ENSO-like interdecadal variability: 1900–93. *J. Climate,* **10,** 1004–1020.